JGR Atmospheres

RESEARCH ARTICLE
10.1029/2021JD035370

Special Section:
Southern Ocean clouds, aerosols, precipitation and radiation

Key Points:

- Macquarie Island Cloud and Radiation Experiment data are used to study seasonal, diurnal, and synoptic variation in surface precipitation
- Rain, ice/mixed, and small particle precipitation occurred year-round, comprising 74%, 16%, and 10% of total accumulation, respectively
- CloudSat 2C-Precip-Column overestimated liquid accumulation and mixed phase occurrence but underestimated light precipitation occurrence

Supporting Information:

Supporting Information may be found in the online version of this article.

Correspondence to:

E. Tansey,
etansey@uw.edu

Citation:

Tansey, E., Marchand, R., Protat, A., Alexander, S. P., & Ding, S. (2022). Southern Ocean precipitation characteristics observed from CloudSat and ground instrumentation during the Macquarie Island Cloud and Radiation Experiment (MICRE): April 2016 to March 2017. *Journal of Geophysical Research: Atmospheres*, *127*, e2021JD035370. https://doi.org/10.1029/2021JD035370

Received 4 JUN 2021
Accepted 16 FEB 2022

Southern Ocean Precipitation Characteristics Observed From CloudSat and Ground Instrumentation During the Macquarie Island Cloud & Radiation Experiment (MICRE): April 2016 to March 2017

Emily Tansey[1], Roger Marchand[1], Alain Protat[2,3], Simon P. Alexander[3,4], and Saisai Ding[5]

[1]University of Washington, Seattle, WA, USA, [2]Australian Bureau of Meteorology, Melbourne, VIC, Australia, [3]Australian Antarctic Partnership Program, Institute for Marine and Antarctic Studies, University of Tasmania, Hobart, TAS, Australia, [4]Australian Antarctic Division, Hobart, TAS, Australia, [5]Ocean University of China, Beijing, China

Abstract A 1-year blended surface precipitation data set using Parsivel disdrometer, surface W-band radar, and tipping bucket measurements is produced for the Macquarie Island Cloud and Radiation Experiment (MICRE) and compared with retrievals from CloudSat (spaceborne 94 GHz radar). Surface precipitation was observed 44% ± 4% of the time between April 2016 and March 2017. Precipitation composed primarily of small particles (diameter <1 mm) occurred about 36% ± 2% of the time, constituting 10% of total accumulation. Remaining precipitation contained enough large particles such that the disdrometer could be used to identify the precipitation type as rain, ice, snow or wet snow. Seasonal and annual statistics on frequency of occurrence and accumulation for each precipitation type observed during MICRE are presented. Most ice and mixed phase precipitation was shallow, originating at a height of 3 km or lower, and occurred most often when Macquarie Island was to the northwest of the nearest cyclonic low-pressure center. In contrast, rain was more often deep and occurred most frequently when the island was to the southeast of cyclonic lows. A weak diurnal cycle in frequency and mean rate was present with a minimum between 12:00 and 14:00 local time and maximum between 03:00 and 06:00 local time. The CloudSat 2C-Precip-Column product missed the lightest precipitation (because the near-surface reflectivity is <-15 dBZ) and overestimated total liquid precipitation and occurrence of mixed phase precipitation, but captured reasonably well the distribution of rain rates for rates >0.5 mm/hr.

Plain Language Summary Understanding the nature of precipitation over the Southern Ocean (SO) is crucial to understanding cloud properties, which climate models struggle to simulate correctly with significant impacts on global climate sensitivity (how much the Earth is likely to warm due to increases in greenhouse gases). Studies assessing the performance of climate simulations rely primarily on satellite measurements and reanalysis of precipitation in remote regions like the SO due to the lack of available surface measurements. However, there are large disagreements between and among satellite and reanalysis products regarding SO precipitation characteristics. This study examines precipitation characteristics obtained from a recent field campaign located at Macquarie Island, in the middle of the SO. The analysis presented here focuses on SO precipitation type (liquid, frozen or mixed) and accumulation, as well as seasonal and storm-related variability. Ground observations from Macquarie Island are also compared to CloudSat satellite precipitation estimates that are a crucial data source for precipitation in the region.

1. Introduction

Previous studies have documented that Southern Ocean clouds, including the wide-spread shallow (low altitude) clouds that dominate the total cloud cover, are frequently precipitating, with liquid, frozen, and mixed phase precipitation all being commonplace (Chubb et al., 2013; Lang et al., 2018, 2020; Mace & Protat, 2018a, 2018b; Wang et al., 2015). Precipitation is a major source of freshwater input into the SO (Pauling et al., 2016) and affects low cloud occurrence and radiative properties directly through microphysical processes, and indirectly through its effects on aerosols, as well as through dynamical and thermodynamical interactions (Wood, 2012). Climate models have historically struggled to simulate accurately top-of-atmosphere radiative fluxes and the surface energy budget of the SO (Bodas-Salcedo et al., 2016; Trenberth & Fasullo, 2010; Schneider & Reusch, 2016). These errors are of profound importance, influencing local and global atmospheric and oceanic circulations

(Ceppi et al., 2012, 2013; Hwang & Frierson, 2013; Kay et al., 2016; Sallée et al., 2013) and global climate sensitivity (Gettelman et al., 2019; Bodas-Salcedo et al., 2019; Zelinka et al., 2020).

Because of the sparseness of surface observations, studies requiring regional knowledge of SO precipitation characteristics typically rely on reanalyses or satellite-based products. Unfortunately, there are large differences between various reanalyses and between different satellite precipitation products in the phase (liquid versus ice), frequency and rate of precipitation, as well as total accumulation over the SO (Behrangi et al., 2014, 2016; Boisvert et al., 2020; Manton et al., 2020). While reanalyses are constrained by observations and often run at finer resolutions than climate models, they use many of the same cloud and precipitation parameterizations used in climate models and suffer from many of the same biases over the SO as climate models (Lang et al., 2018; Naud et al., 2014). Satellite-based products, including the GPCP climatology (Huffman & Bolvin, 2013) and CMAP (Xie & Arkin, 1997) are widely used, as are retrievals based on spaceborne radar from the NASA CloudSat W-band radar and NASA Global Precipitation Measurement (GPM) mission's Ku/Ka-band radars (Behrangi et al., 2012, 2014; Hayden & Liu, 2018; Skofronick-Jackson et al., 2017). GPCP and CMAP both make heavy use of retrievals based on satellite infrared and passive microwave measurements, and differ substantially with retrievals based on spaceborne radar over the SO (Behrangi et al., 2012, 2014, 2016). For instance, Behrangi et al. (2014) found that GPCP overestimates daily precipitation by about 0.5–1.5 mm from a baseline of about 2.5 mm (an error range of 35–50%) over the SO between 50°S and 60°S (see their Figure 4), as compared with a satellite precipitation product Behrangi and colleagues developed that includes CloudSat retrievals, while CMAP underestimated precipitation by a similar amount. Arguably the best available source of data on precipitation characteristics over the SO are based on CloudSat radar observations because these estimates are based on vertically resolved measurements, have greater sensitivity to light precipitation than lower frequency radar or passive infrared or microwave measurements, and extend to about 82°S (GPM is limited to about 65°S). However, the CloudSat measured reflectivities are affected by ground clutter, which severely corrupts the measurements within about 750 m of the surface (Marchand et al., 2008), and provide very limited information regarding the phase of precipitation. Most precipitation phase information relies on the radar column having identifiable melting layers in regions with stratiform precipitation (Haynes et al., 2009). CloudSat measurements also do not allow one to discriminate easily between cloud and light precipitation because radar reflectivities less than about −15 dBZ can be due to either cloud or precipitation size particles.

Surface measurements of precipitation over the open SO are largely limited to a few island sites and research cruises (e.g., Klepp et al., 2018; Mace & Protat, 2018a, 2018b; Manton et al., 2020). Of particular note are surface meteorological measurements at Macquarie Island, including tipping bucket rain gauge observations of surface accumulation stretching back to 1948. These measurements have been used in studies on climate and climate change, as well as in the evaluation of climate and weather prediction models (Adams, 2009; Hande et al., 2012; Lang et al., 2018; Wang et al., 2015).

Macquarie Island is located at 54.5°S, 158.9°E and has a small research station operated by the Australian Antarctic Division (AAD) and staffed year-round, in part by the Australian Bureau of Meteorology (BoM). Between March 2016 and March 2018, the U.S. Department of Energy Atmospheric Radiation Measurement (ARM) program, AAD and BoM collaborated in deploying a variety of ground instrumentation to Macquarie Island during the Macquarie Island Cloud and Radiation Experiment (MICRE). MICRE was part of several interconnected experiments that took place during this time, described in detail by McFarquhar et al. (2021). The MICRE deployment included a Parsivel-2 disdrometer and Vaisala CTK-25 ceilometer (supplied by ARM), the W-band Bistatic rAdar SysTem for Atmospheric studies (BASTA) cloud radar for the first year April 2016 to March 2017 (supplied by BoM), the AAD depolarization lidar during winter 2016 and again from April 2017 to March 2018 and a Vaisala CL-51 ceilometer (University of Canterbury) which operated for the full April 2016 to March 2018 campaign. In this article, the Parsivel-2 disdrometer, ceilometer, and cloud radar measurements from the first year of MICRE are blended with tipping bucket measurements at the site to determine the surface precipitation rate, thermodynamic phase, and particle size distribution.

A description of the data sets and blending approach is given in Section 2, followed by an examination of seasonal, diurnal, and synoptic variations observed during MICRE in Sections 3–5, respectively. In Section 6, we compare the MICRE blended data with CloudSat retrievals, with discussion in Section 7 and a summary of key results given in Section 8.

We stress that the surface data is from a single site and covers a period that is just under 1 year in duration (and as will be discussed in Section 2, the analysis is restricted largely to periods where the radar, disdrometer and tipping bucket all have high quality data, about 80% of the 12 months). Consequently, these data do not characterize interannual or longer timescale variability. Furthermore, the observation period is somewhat anomalous in that the longer-term tipping bucket record at the observation site shows that the MICRE summer months (December 2016, January and February 2017) have the highest total accumulation in the last 14 years. Therefore, inferences regarding the broader SO climatology should be undertaken with caution and arguably done in the context of satellite and other surface measurements. We will return to this topic in the discussion section of the paper.

2. Data and Methods

2.1. MICRE Blend: Disdrometer, W-Band Radar, and Tipping Bucket

This work blends measurements from a Parsivel disdrometer, ceilometer, and W-band radar together with tipping bucket measurements to form a detailed description of surface precipitation phase, rates, and particles size distributions. All data used in this study, including the blended precipitation data and synoptic environment data, are available publicly as described in the acknowledgments.

The Parsivel disdrometer is a laser-based optical precipitation sensor developed by OTT Messtechnik. It consists of two hooded segments: one for the laser transmitter and one for the photodiode detection receiver. These are separated by a distance of 180 mm. Laser light is spread horizontally to form a beam 30 mm wide and 1 mm thick, creating a detection area of 180×30 mm^2 through which precipitating particles fall. Raw Parsivel measurements consist of a time-dependent voltage signal as particles pass through the laser beam. To a large extent, this signal is dampened in proportion to beam blockage. Particle equivalent diameter is estimated by a proprietary vendor provided algorithm, key aspects of which are discussed by Battaglia et al. (2010). The primary output available to us is joint histograms of estimated particle size and particle velocity (so called size-velocity spectra) obtained from the voltage signal of many particles that have passed through the laser beam. Nominally, the instrument detects liquid particles with diameters between 0.2 and 25 mm, but bins below about 1 mm are known to experience undercounting (Löffler-Mang & Joss, 2000; Tokay et al., 2013). In particular, we found that undercounting was apparent (relative to tipping bucket and radar retrievals) during periods when the laser amplitude was below its nominal operational value. In addition to the instrument's lack of sensitivity to small particle precipitation, major limitations of the Parsivel include (i) its susceptibility to wind-induced errors, (ii) the presence of "margin fallers" or particles that pass partially through the beam at one of the edges (Battaglia et al., 2010), and (iii) the fact that (as far as we can ascertain) the vendor's code lacks any sort of density correction for frozen particles, causing systematic overestimation in the vendor's precipitation rates for frozen precipitation. The exact cause of wind-driven errors is unclear but splashing droplets off the instrument housing and impacts from turbulent air motions within the beam are suspected (Friedrich et al., 2013). The vendor software nominally provides "weather codes," which indicate when drizzle, rain, ice pellets, snow or some mixture of these precipitation types is detected. A number of studies have discussed considerations that go into determining the particle phase (Battaglia et al., 2010; Löffler-Mang & Joss, 2000; Raupach & Berne, 2015). Broadly speaking, particle equivalent size compared to its fall speed is used to characterize phase. Details of the vendor weather code algorithm are also proprietary, and problematically for MICRE, a data logger error caused much of the weather code output to be lost.

The above factors prompted us to reprocess the raw (level 2) size-velocity spectra via a new retrieval we developed, referred to in the following as the *Parsivel Improved Rates and Types (PIRAT)* algorithm. The PIRAT algorithm removes contributions from wind and margin fallers, accounts for diameter overestimation and fall speed underestimation due to wind, identifies precipitation type (as rain, ice, wet snow, dry snow or small), determines the particle size distribution and accounts for particle density in the precipitation rate calculation. The precipitation type is determined based on four expected size-velocity relationships for rain, ice, wet snow, and dry snow. This identification requires that particles larger than 1 mm be present because particles smaller than about 1 mm do not fall at sufficiently different velocities for differences in the density to be distinct. Size spectra without a sufficient number of large particles are simply classified as being "small." A detailed description of the algorithm, including the size-velocity relationships, is given in Supporting Information S1. The algorithm is written in Python and is now available on GitHub at https://github.com/etansey/PIRAT_algorithm. In the present

application, we reduced the original 1-min temporal instrument output rate to 5 min, which we found was necessary to get sufficient counts during periods with light precipitation.

In the Supporting Information S1 (Section S5), we compare near-surface radar mean Doppler velocities to PIRAT corrected particle fall velocities for each particle type. The comparison shows that PIRAT velocities and types are largely consistent with the Doppler radar velocities, though the data also suggest that wet snow and ice identifications may contain a significant number of events which should have been classified as snow or small particle dominated events.

The zenith pointing W-band Bistatic rAdar SysTem for Atmospheric studies (BASTA) cloud radar (Delanoë et al., 2016) was used to obtain vertical profiles of cloud reflectivity and Doppler velocity during MICRE. A pointing accuracy better than 0.1° is achieved using very accurate inclinometers to adjust the pointing direction of the antennas with respect to the frame of the instrument and the frame of the instrument to the horizontal. The measured radar reflectivity and mean Doppler velocity were used to estimate the precipitation rate and mean particle size following the retrieval approach of Frisch et al. (1995). In this retrieval, the precipitation particle size distribution is represented by a lognormal distribution. The BASTA radar did not measure the Doppler spectral width, from which an estimate for the lognormal distribution width might be obtained. Rather, in our application, the precipitation size distribution is assumed to have a lognormal width of 0.35, following the "in cloud" approach of Frisch et al. (1995). This leaves two free parameters which are determined in the retrieval from the measured reflectivity and estimated particle fall velocity. The true lognormal width is not constant, but varies with typical values between about 0.15 and 0.45 for drizzling marine stratocumulus. Values of 0.15 and 0.45 result in a retrieved mean particle size that is 90% larger or 40% smaller, respectively, and precipitation rates that are as much as 25% smaller or larger, respectively. Another significant source of uncertainty arises from estimating the particle fall velocity from the measured Doppler velocity. We estimate the fall velocity using conditional averaging of the measured Doppler velocity (conditioned on the measured reflectivity) following Orr and Kropfli (1999). The minimum number of measurements required in the averaging results in a nominal uncertainty in the fall velocity of less than 0.1 m/s. Uncertainty in the retrieved mean particle size due to a 0.1 m/s uncertainty in the fall velocity is ±5.4 μm, and −30% to +70% in the precipitation rate (with the largest rate errors being associated with the smallest mean particle size allowed, about 25 μm). Of course, individual events could have biases that are larger than this. For example, if larger reflectivities are preferentially associated with downdrafts, the estimated fall velocity might be biased large at these larger reflectivities. In the blend product, the ZV retrieval is only used when the accumulated precipitation is too light to be measured by the tipping bucket, and so downdrafts are not likely to be a serious problem. Another factor that might bias the fall velocities is deviations in the radar pointing from true nadir. Pointing errors would cause horizontal motions of the precipitation to contribute to the measured Doppler velocity. For cases with non-to-lightly precipitating stratocumulus, we find mean in-cloud vertical velocities are reasonably small (typically less than 0.25 m/s), suggesting there is little error in the velocities due to off-zenith pointing. Ultimately, we flag retrievals with estimated fall velocities below 0.3 m/s as unreliable and these retrievals are not included in the later analysis. The radar measurements used in the retrieval correspond to an altitude range near the surface, but not at the surface. Specifically, measurements are averaged between about 150 and 250 m. Measurements below 150 m are not used because they are sometimes contaminated by surface clutter. We effectively assume that reflectivity and velocity will have changed minimally between 250 m and the surface. Some of the time, especially for the very lightest rain rates, this will not be a good assumption and some amount of virga will be included in our statistics. We will return to this topic in the concluding discussion. Except where specifically noted otherwise, we include only radar retrievals where cloud base estimated from the ceilometer is above 250 m.

The initial radar calibration was adjusted by 1.1 dBZe after comparison to CloudSat following the approach of Protat et al. (2011). It was further evaluated for consistency with PIRAT corrected precipitation particle size distributions (PSDs) during periods with light rainfall (reflectivity <10 dBZe) using T-matrix calculations. This comparison found agreement between the radar reflectivity and PIRAT PSDs to better than 2 dB. The radar retrieval relies on the assumption of Rayleigh scattering, meaning that particles are small compared to the radar wavelength. For W-band radar, Rayleigh scattering is a good approximation for liquid particles with diameters of 0.5 mm or smaller, with deviations in the backscatter from Rayleigh scattering becoming significant by the time one reaches 1 mm (Tridon & Battaglia, 2015). Consequently, the radar ZV retrieval is only reliable for light

Table 1
Percent of Good Data, Mean Precipitation Rates, and Frequency of Precipitation by Season

	% Good blend data	Blend mean rates ± standard error (mm/hr)	TB (full record) mean rates ± standard error (mm/hr)	Radar (full record)% Time detection at 150 m	Radar (good-quality blend data)% Time detection at 150 m
Summer (DJF)	64%	0.195 ± 0.095	0.206 ± 0.023	35.9% ± 2.7%	31% ± 2.7%
Fall (MAM)	73%	0.155 ± 0.093	0.154 ± 0.017	42% ± 2.7%	40.9% ± 2.8%
Winter (JJA)	91%	0.165 ± 0.081	0.140 ± 0.011	43.4% ± 2.4%	41.2% ± 2.4%
Spring (SON)	92%	0.135 ± 0.058	0.116 ± 0.010	36.8% ± 2.5%	36.4% ± 2.6%
Annual	80%	0.160 ± 0.040	0.154 ± 0.015	39.5% ± 2.6%	37.4% ± 2.6%

precipitation composed of small particles. In this way, the radar supplements the Parsivel measurements well because, as stated previously, the disdrometer often misses particles below about 1 mm in diameter.

We blend the PIRAT data with the radar retrievals for near-surface precipitation and tipping bucket measurements. A full description is given in the Supporting Information S1, but briefly, the blending algorithm first synchronizes the radar retrievals to PIRAT, storing average radar rain rates and particle sizes over 5 min. Periods where the radar retrieval is of low quality are flagged and retrieved rates are not used in the analysis (except where specifically stated otherwise). Likewise, periods where the ceilometer cloud base estimates are missing are flagged and not used in the analysis (except where specifically stated otherwise). The ARM ceilometer is used primarily in the retrieval and supplemented by the University of Canterbury ceilometer for missing periods. Surface meteorological measurements at the site, including the tipping bucket, are recorded at 1-min resolution and include temperature, wind speed, wind direction, and relative humidity. The tipping bucket tips occur at every 0.2 mm of liquid accumulated. In the blend product, the PIRAT particle size distributions are scaled such that the resulting PIRAT accumulation matches the tipping bucket accumulation over 2-hr periods. The tipping bucket is susceptible to systematic wind errors of its own for precipitation events containing smaller drops and higher wind speeds (Nešpor & Sevruk, 1999; Sevruk, 1996). Snow is commonly undercounted by tipping buckets because the gauges must be heated to melt snow and tip, but heating causes evaporation. This may cause even more undercounting than wind during snowfall, which also causes errors as snow can blow in and out of the gauge (Savina et al., 2012; Zweifel & Sevruk, 2002). We have not undertaken any corrections to the tipping bucket data, and the blend accumulations (during periods when precipitation is sufficient to register a tip) are as good (or bad) as the tipping bucket measurements on which they are based. The radar fills in periods when precipitation is either too light to be detected by the Parsivel or when the PIRAT precipitation type is "small" and PIRAT underestimates the precipitation rate relative to the radar.

Except where noted otherwise, the data analysis is based only on periods where good-quality blend data exists. This requires good tipping bucket, disdrometer, radar, and ceilometer data. Table 1 lists percentages of good data for each season and annually, along with the mean precipitation rate (equivalent to the total accumulation divided by the number of hours of good data, regardless of whether or not it is precipitating) for the full tipping bucket record and the good-quality blend data. Also listed is the fraction of time that there is a radar detection with a reflectivity of at least −20 dBZe at 150 m above the surface (regardless of whether or not the detection is due to precipitation or low cloud), first for the entire radar record, and then restricted to periods with good-quality blend data. The rejected or poor-quality periods include both clear and precipitating periods, and are frequently caused by instruments or data loggers going down and needing to be manually reset, resulting in dropouts with durations that last days. In particular, there is a 20-day gap in the tipping bucket data record beginning in late December 2016 that is responsible for the relatively low amount of good-quality data in the summer period (DJF). The missing days are not likely to bias the data, but other factors do have this potential; for example, removing data where the radar ZV retrieval fails to obtain a good velocity estimate or removing data where there are large mismatches between the tipping bucket and disdrometer data. Specifically, we exclude 2-hr periods when the tipping bucket tips several times but the Parsivel records no precipitation whatsoever. Nonetheless, the average precipitation rates in Table 1 indicate that there is little if any significant difference between the blend seasonal mean precipitation rates and those from the full tipping bucket record. And likewise what bias does exist in the frequency of near-surface radar detections is small and comparable to the 1-sigma sampling uncertainty.

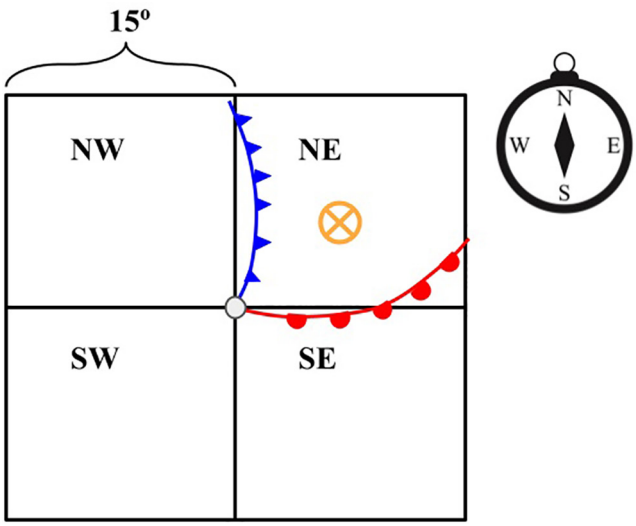

Figure 1. Geographic illustration of quadrants with respect to the storm center. For example, if Macquarie Island is located at the position marked by the orange cross, the island is defined to be in the northeast (NE) quadrant of the low. If Macquarie does not fall within a 30° × 30° region centered on the closest low, it is categorized as "far" from the storm.

2.2. Synoptic Environment Data

In this study, we characterize the synoptic environment by the distance to the nearest extratropical cyclone (low-pressure) center, as well as the quadrant in which the MICRE site resides relative to the nearest low-pressure center using the NASA Modeling, Analysis, and Prediction Climatology of Midlatitude Storminess (MCMS) database (Bauer et al., 2016). In the MCMS database, storm centers are defined by the location of minima in the ERA-Interim (1.5° horizontal resolution) sea-level pressure. The low-pressure minima must meet criteria based on hemisphere, topography, and season, and are tracked over time. A detailed description of the algorithm is given by Bauer et al. (2016). The data are categorized according to the quadrant in which Macquarie Island lies relative to the closest low, as depicted in Figure 1. If Macquarie does not fall within a 30° × 30° region centered on the closest low, it is categorized as being "far."

2.3. CloudSat CPR Products

CloudSat, a 94-GHz nadir-pointing radar, was launched into a sun-synchronous polar orbit as part of the A-Train satellite constellation on April 28, 2006. In spite of some reduction in instrument sensitivity, battery limitations that restrict observations to daylight conditions and other problems, it continues to provide useful observations to the remote sensing community (Stephens et al., 2012). In this study, we examine the current CloudSat operational precipitation products (revision R05), namely, 2C-Precip-Column (Haynes et al., 2009), 2C-Rain-Profile (Lebsock & L'Ecuyer, 2011), and 2C-Snow-Profile (Wood et al., 2014). These data are freely available from the CloudSat Data Processing Center (DPC; http://www.cloudsat.cira.colostate.edu/). Full descriptions of these products are given in the above references, with additions and changes for the latest version (R05) documented on the website.

The first of the CloudSat precipitation algorithms to be applied is 2C-Precip-Column, hereafter just 2C-Precip. 2C-Precip identifies precipitation in the vertical radar beam, hereafter referred to as the column, with three confidence levels: "certain," "probable," and "possible," based on an estimate for the (attenuation corrected) near-surface reflectivity factor. The lowest confidence precipitation category requires a near-surface reflectivity between −15 and −7.5 dBZ for liquid ("rain possible"), or −15 and −5 dBZ for frozen ("snow possible") (Haynes et al., 2009). The column is flagged as "rain probable" for near-surface reflectivity between −7.5 and 0 dBZ, and "rain certain" for greater than 0 dBZ. Similarly, "snow certain" is assigned for frozen precipitation columns with reflectivity greater than −5 dBZ. The CloudSat CPR suffers significant limitations from ground clutter effects, that is, interference generated by the interaction of the radar pulse with the surface. The ground clutter makes it difficult to make meaningful measurements of hydrometeor reflectivity closer than about 750 m above the surface (Marchand et al., 2008), and consequently the above thresholds are typically applied to the CloudSat measurement which is 750 m to 1 km above the surface. The precipitation phase is categorized as being liquid, mixed phase or snow. The categorization is largely based on ECMWF temperature profiles in combination with a model for precipitation melting. The algorithm tries to identify when a melting layer is present from the observed reflectivity profile, and otherwise uses the ECMWF profile freezing level. The melting model assumes a lapse rate of 6°C km^{-1} and provides an estimate for the "melt fraction," with values between 0 and 1, where 1 means liquid precipitation. A more complete description of the algorithm can be found in Haynes et al. (2009). Radar columns with a melt fraction greater than 0.9 are treated as liquid and the 2C-Precip algorithm provides an estimate for the surface rain rate in this situation, while for mixed phase or completely frozen precipitation, no precipitation rate is given in 2C-Precip. For those radar columns with a melt fraction >0.9 that are also rain certain (near-surface reflectivity >0 dBZ), the 2C-Rain-Profile algorithm provides a vertical profile of rain rates (not only the surface rain rate). The precipitation retrieval in 2C-Rain's algorithm differs substantially from 2C-Precip. 2C-Precip infers the presence of surface rain from a single measurement of the path integrated attenuation (PIA) assuming a uniform rain column, whereas 2C-Rain uses a PIA constraint while also deriving a rain profile from the radar reflectivity and estimating evaporation below-cloud base. In the event that the melt

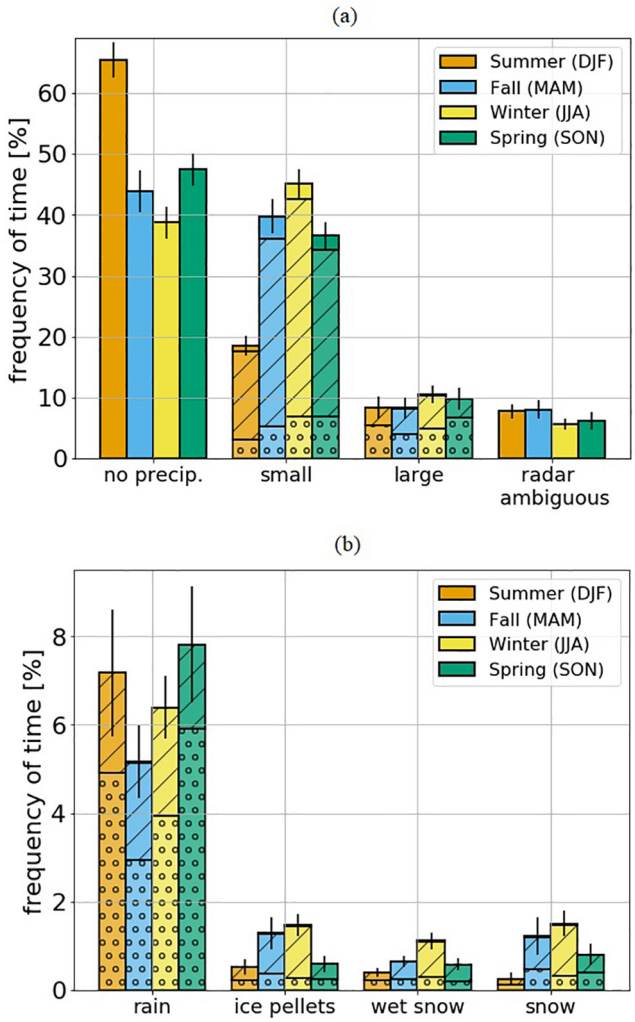

Figure 2. (a) Frequency of occurrence (percent of the time) of small particle (near-surface), large particle and no detectable precipitation, as well as ambiguous cases. (b) Frequency of large particle precipitation occurrence broken into phase categories. Solid colors = no precipitation depth was retrieved; dotted bars = deep (>3 km); cross hatched bars = shallow (<3 km). The thin lines at the top of each bar show the uncertainty in the estimated frequency of occurrence due to sampling (see text).

fraction is less than 0.1, the 2C-Snow-Profile algorithm likewise retrieves a precipitation rate profile (assuming fully frozen ice-only precipitation). No operational precipitation retrieval is currently run when the estimated melt fraction is between 0.1 and 0.9.

The 5-min timescale used in our blended MICRE data set is roughly equivalent to a horizontal spatial scale of 3–6 km (as wind speeds are typically between 10 and 20 m/s). This is larger than the effective CloudSat radar footprint (about 1.4 × 1.7 km, Marchand et al., 2008). However, we have repeated much of the analysis presented here by averaging neighboring CloudSat radar columns and find this makes no noteworthy difference in the results. This is not surprising for several reasons including that the CloudSat hydrometeor detection assumes hydrometeor occurrence is correlated over several pixels and hydrometeors that are isolated to a single radar column are not likely to be accepted as good detections.

3. Seasonal Variations in Surface Precipitation

We look first at the annual and seasonal frequency of occurrence of precipitation. Figure 2 shows the percent of time that precipitation is detected in each season using the MICRE blended precipitation data. In Figure 2 and later figures, the thin black lines at the top of each bar provide an estimate for the sampling uncertainty. Specifically, we calculate a daily frequency of occurrence for each precipitation type in each day (based on the five-minute blended retrieval) and plot here the average frequency of occurrence and the sampling uncertainty (given by the standard deviation divided by the square root of the number of days). Thus, the estimated uncertainty treats each day as a single independent sample. This is conservative regarding the impact of short timescale variability but does not account for the effects of variability on long time scales (e.g., annual variability) nor does it include any biases that might stem from the retrieval.

We find the total frequency of precipitation occurrence for fall (MAM) was 48% ± 5%, winter (JJA) was 56% ± 4%, spring (SON) was 46% ± 4%, and summer (DJF) is 27% ± 3%, with an annual average of 44% ± 4%. The total frequency of precipitation is dominated by small particle precipitation, meaning precipitation whose particle size distribution contains few particles larger than 1 mm (such that the particle phase could not be determined from the disdrometer measurements). However, following Mace and Protat (2018a, 2018b), we have examined lidar depolarization measurements below-cloud base for individual cases, and find that the small particle precipitation is predominantly liquid phase. As will be shown in Section 6, small particle precipitation has precipitation rates that are typically less than 0.1 mm/hr.

Relative to the total frequency of occurrence, a small fraction of the data is identified in Figure 2a as "radar ambiguous." This occurs when the radar detects hydrometeors near the surface, but it is ambiguous as to whether the detected hydrometeors are precipitation, low cloud/fog or possibly blowing sea spray. Specifically, this category corresponds to conditions where the radar detects hydrometers with a reflectivity <−15 dBZ between 150 and 250 m above the surface, but the location of cloud base from the ceilometer was below 250 m. The radar is unable to detect hydrometeors below about 150 m because of surface clutter and signal leakage between the transmitting and receiving antennas. It is important to note that small particle frequency of occurrence includes radar-detected drizzle that has gotten within 250 m of the surface but could evaporate before reaching the surface. In short, this is the near-surface precipitation frequency of occurrence. We discuss this further in the concluding section.

If one considers only large particle precipitation, the frequency of occurrence is much smaller and becomes 8% ± 2% for fall (MAM), 10% ± 1% for winter (JJA), 10% ± 2% for spring (SON), and 8% ± 2% for summer (DJF), with an annual average of 9% ± 2%. Wang et al. (2015) found using 3-hourly tipping bucket data from 2003 to 2011 that precipitation occurred at Macquarie Island about 36% of the time, and of this, about 30% of the time the precipitation rate was light (less than 0.5 mm/hr). The MICRE blend frequencies are not directly comparable to these tipping-bucket-only frequencies because of the different timescales and minimum detectable precipitation rates, but this does show that light precipitation dominates the frequency of occurrence at both time-space scales.

In fall, winter and spring the total frequency of both large and small particle precipitation is comparable, with small particle precipitation occurring 34%–47% of the time and large particle precipitation occurring 7–12% of the time. The summer is markedly different from fall, winter, and spring, with much lower occurrence of small particle precipitation (19% ± 2%). A further breakdown of the seasonal cycle of precipitation occurrence by the phase of large particles is shown in Figure 2b. Not surprisingly, in winter when temperatures are lowest on average, the occurrence of large particles identified as ice, snow or wet snow is largest. Note that the sum of the ice and mixed phase categories in winter is 4% ± 0.7% which is comparable to the occurrence of rain at 6% ± 0.7%. Regardless, it is noteworthy that both liquid and frozen precipitation occur in all seasons.

Figure 2 also provides some insight into the vertical depth of the systems producing the observed precipitation. For the small and large particle categories, hatching in Figure 2 indicates the fraction of time that precipitation is deep (the precipitation extends to altitude >3 km; dotted hatching) or shallow (extent is <3 km; cross hatching). Specifically, deep versus shallow precipitation is determined by applying a 5-min mean to the W-band radar reflectivity profiles (averaging only when reflectivity is greater than the radar noise level as determined by the radar hydrometeor mask). Precipitation depth is defined as the height (going up from the surface) where there is a continuous mean reflectivity signal of −15 dBZ or greater. Unhatched area in Figure 2 indicates the fraction of time where no precipitation depth was available. Missing depths occur primarily when 5-min radar averaging indicates that surface precipitation is occurring, but the mean reflectivity profile remains below −15 dBZ. Visual inspection of individual events shows that missing depths are primarily associated with shallow cloud systems. Also somewhat problematic is that attenuation (due to both liquid water on the radar radome and in the atmosphere) affects the measured reflectivity and this can lead to deep precipitation systems being misclassified as shallow events. However, we find this only typically occurs when the surface rain rate exceeds about 5 mm/hr, which is relatively rare (occurring less than 1% of the time) and consequently, attenuation can only modestly affect the shallow and deep statistics presented in Figure 2. Nonetheless, this uncertainty is not trivial, especially concerning the frozen precipitation types, where the frequency of deep could be twice as large as it appears in Figure 2.

As one might expect, small particle precipitation is primarily associated with shallow precipitation, while the frequency of large particle precipitation is roughly equally split between shallow and deep. Perhaps surprisingly, however, Figure 2b shows that ice and mixed phase precipitation are more frequently originating below 3 km. CloudSat retrievals, which are discussed in Section 6, also show that ice and mixed phase precipitation frequently originate from shallow clouds.

Turning attention to total accumulation, Figure 3 and Table 2 show the relative contribution of each precipitation type in each season to the total accumulation based on the blend data. By construction, the columns in Figure 3 sum to 100%. Rain (large particle liquid precipitation) contributes more to the total accumulation than small particle, ice or mixed phase precipitation in all four seasons, comprising 74% of the annual accumulation. Of this 74%, rain originating deep (>3 km) in the atmosphere is responsible for 47.5%, while shallow rain contributes 26.5%. The deep rain contribution is higher in all seasons. During MICRE summer precipitation contributed the most to the annual accumulation (29% of annual total accumulation). However, we note that this is due to summer (DJF) and winter (JJA) being unusually wet, which we discuss in more detail in the concluding section.

While contributing less to the total accumulation than rain, small particle precipitation is nonetheless significant, contributing ∼10% to the total, with the contribution being largest in winter and smallest in summer. Ice and mixed phase precipitation contribute less than rain but more than small particle precipitation to the total annual accumulation (16%). Ice and mixed phase accumulation were largest in fall (8%). While shallow ice and mixed phase precipitation occur more frequently than deep in the fall, deep precipitation contributes more to

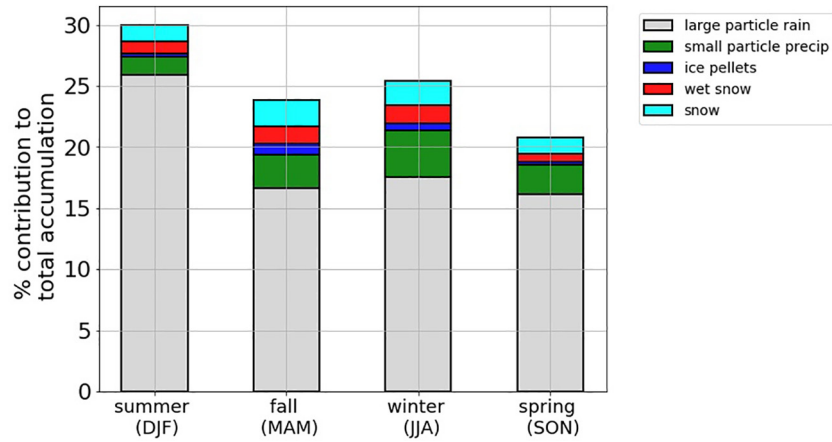

Figure 3. Percent contribution to annual accumulation at Macquarie Island, broken into seasons and thermodynamic phase.

accumulation. We discuss the depth of ice and mixed phase precipitation further in Section 6 with respect to CloudSat observations.

4. Diurnal Variations in Surface Precipitation

The diurnal cycle of the annual precipitation on an hourly scale is shown in Figure 4. The morning and afternoon CloudSat overpasses nearest to the site occur at approximately 02:00 local time (LT) and 15:00 LT once every 16 days, and pass within about 0.75° of the site. The times of CloudSat overpasses are indicated by red stars in Figure 4. It turns out that the CloudSat overpasses take place at times of day when rates and frequencies at Macquarie Island are very close to the daily mean values, and consequently, there is likely little diurnal error associated with the CloudSat measurements. We will examine CloudSat retrievals and sampling uncertainties in Section 6.

In Figure 4, the frequency of occurrence is given in the left column and time-mean precipitation rate (accumulation divided by the total time precipitating with good-quality data) in the right column. The top row (Figures 4a and 4b) is restricted to precipitation rates >0.5 mm/hr and the bottom row (Figures 4c and 4d) is restricted to rates <0.5 mm/hr. Precipitation rates below 0.5 mm/hr are dominated by small particles. Error bars in Figure 4 show the 1-sigma sampling uncertainty in the hourly mean (standard deviation divided by the square root of the sample size, ~320 days). While sampling uncertainty is noteworthy (these results are based on only 1 year of measurements), the data are sufficient to discern a broad cycle in the diurnal variability of precipitation. All four panels show a daily minimum between 12:00 LT and 14:00 LT. A bootstrap resampling hypothesis test applied to the diurnal range (daily maximum minus minimum) indicates that the diurnal differences shown in all four panels are significant at the 95% confidence level (see Supporting Information S1). We note that the spike at 11:00 LT in Figure 4b is likely a result of sampling uncertainty. There are 24 hr and it is more likely than not that at least one of these 24 samples will have a value that is 2-sigma too large or too small (sigma is shown by the error bars). The same data are presented on a 3-hourly scale in the Supporting Information S1, and likewise test positive for a statistically significant diurnal cycle. For the period analyzed and for precipitation with rates >0.5 mm/hr, the occurrence and mean rate of precipitation peak in the early morning at about 06:00 LT. While there is a somewhat larger occurrence and mean rate in this category after the 12–14:00 LT minimum, the occurrence and mean rate remain below that found near 06:00 LT, and there is no distinct afternoon peak in mean rate. Precipitation with rates <0.5 mm/hr occurs much more frequently than rates >0.5 mm/hr, consistent with the earlier seasonal analysis of small and large particle precipitation occurrence. There is a greater occurrence and mean rate of light precipitation after 15:00 LT, which continues overnight with a peak near 03:00 LT and a possible second peak around 09:00 LT (Figure 4c). Taken together, increases in total precipitation after 12–14:00 LT manifest principally as an increase in light precipitation rates (<0.5 mm/hr) until about 21–23:00 LT, after which heavier precipitation rates (>0.5 mm/hr) comprise an increasingly large fraction of the total precipitation, with the early morning peak in light precipitation occurring a few hours before the peak in heavier precipitation (03:00 LT as compared to 06:00 LT).

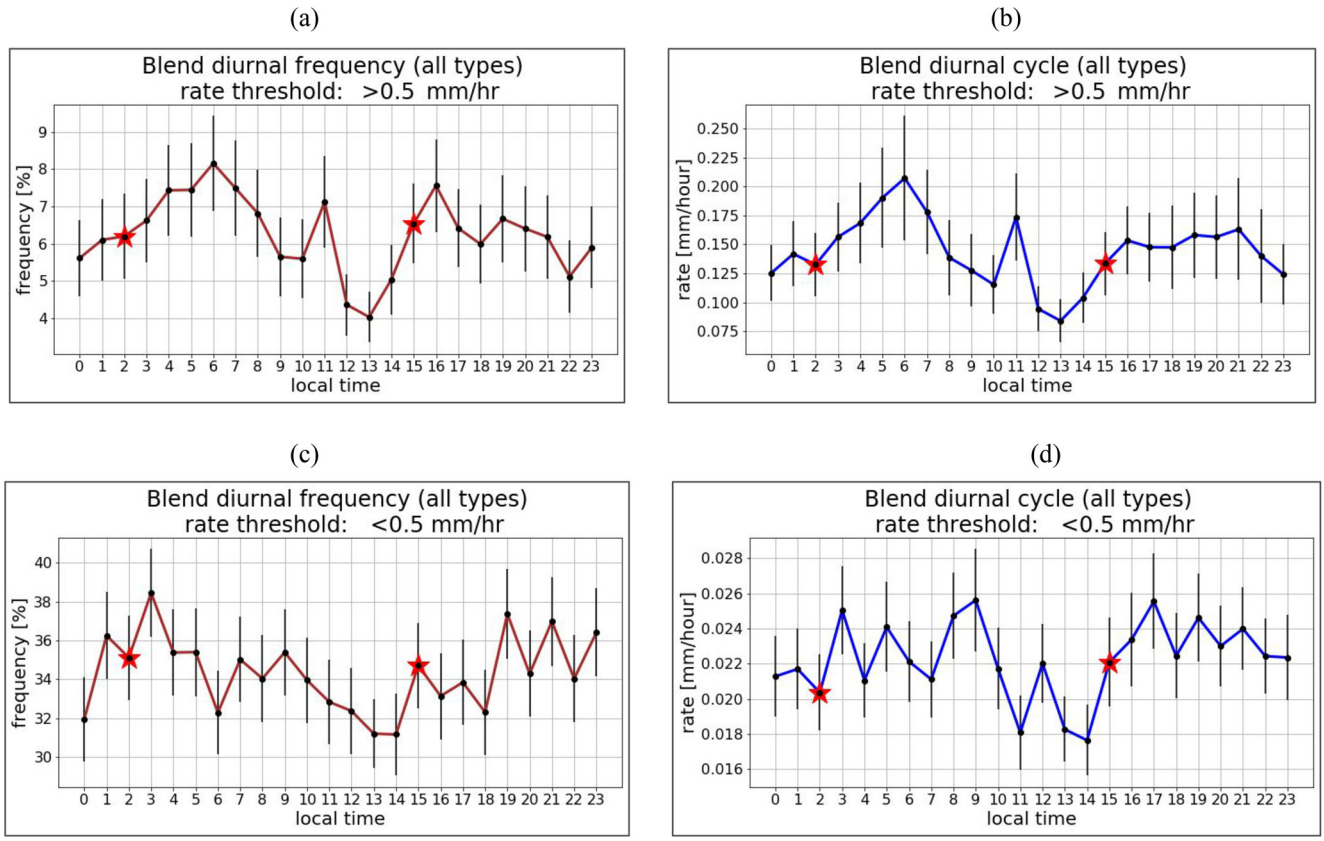

Figure 4. Diurnal cycle of precipitation during Macquarie Island Cloud and Radiation Experiment (MICRE). The diurnal cycle is broken into frequency of precipitation occurrence (a, c) and the average hourly precipitation rate (b, d), and into contributions from precipitation rates >0.5 mm/hr (a, b) and rates <0.5 mm/hr (c, d). Black lines show the 1-sigma sampling uncertainty (standard deviation of hourly means divided by the square root of the number of days sampled) and red stars correspond to the approximate times of CloudSat overpasses.

To be clear, the statistical test for diurnal significance that we have applied establishes only that the difference between the minimum (which occurs between 12:00 and 14:00 LT) and the peak (in both occurrence and mean precipitation rate) are significant relative to day-to-day variability for the observational period. It does not demonstrate that the timing of the peak is robust. For example, we cannot claim with any reasonable confidence that the maximum for light precipitation is 06:00 LT rather than 03:00 LT or even 23:00 LT. The sample size is insufficient to establish the time of the peak with confidence. Nor does the statistical test demonstrate anything about the timing or even the presence of a diurnal cycle outside of the MICRE period. However, in their examination of the longer Macquarie tipping bucket record from 1998 to 2016, Lang et al. (2020) find a minimum in the mean (3-hourly) precipitation rate near 14:00 LT and a maximum in the mean rate in the early morning near 05:00 LT, with this pattern being most prominent for "moderate" precipitation (meaning when the 3-hourly mean rate was between 0.5 and 1.5 mm/hr; see their Figure 3). We also find a similar magnitude in the diurnal cycle to that reported in Lang et al. (2020), with the size of the variation (defined as the daily maximum minus minimum) being about 0.01 mm/hr (for both light rates <0.5 mm/hr and heavier rates >0.5 mm/hr). While not definitive, this suggests that at least the presence of an early afternoon minimum is characteristic for Macquarie Island.

Overall, the observed diurnal characteristics are consistent with those expected for shallow marine stratocumulus, where absorption of solar radiation during the daytime offsets the effect of cloud top longwave radiative cooling and thereby reduces the strength of boundary layer circulations,

Table 2
Percent Contributions to Annual Accumulation by Deep-Originating and Shallow-Originating Large Particle Precipitation (Rain and Ice/Mixed Phase) and Small Particle Precipitation

	Rain (deep | shallow)	Ice/mixed phase (deep | shallow)	Small (deep | shallow)
Summer (DJF)	16.9% | 8.5%	1.5% | 1.1%	0.5% | 0.9%
Fall (MAM)	9.5% | 8.2%	5.1% | 2.6%	0.4% | 2.0%
Winter (JJA)	9.8% | 6.3%	1.2% | 2.5%	0.7% | 2.8%
Spring (SON)	11.3% | 3.5%	1.0% | 1.0%	0.7% | 1.5%
Annual	47.5% | 26.5%	8.8% | 7.2%	2.3% | 7.2%

Note. Percentages sum to 99.5%, With a very small fraction coming from precipitation with an uncertain depth (no radar depth retrieved).

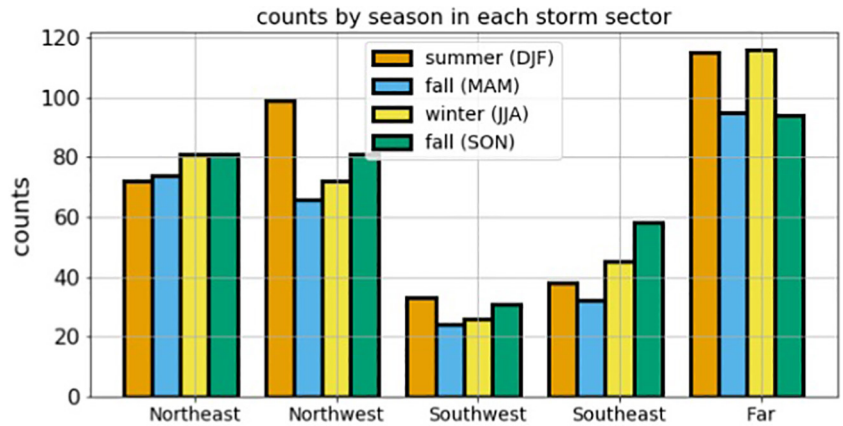

Figure 5. Distribution of synoptic categories, broken into seasons. Counts on the vertical axis indicate the number of 6-hr periods that fall into each category in each season.

cloud amount and the precipitation rate (Wood, 2012), broadly leading to overnight or early morning peaks in precipitation in marine environments (Sui et al., 1997; Tao et al., 1993), although the strength of this cycle varies globally (Yang & Smith, 2006).

Regarding seasonal variations in the diurnal cycle observed during MICRE, uncertainty due to the small sample size of 1 year is too high to draw confident conclusions (figures not shown). The diurnal cycle at heavier rates (>0.5 mm/hr) does appear to be strongest in summer, but the statistical confidence is low. Using the longer Macquarie Island tipping-bucket-only data set, Lang et al. (2020) do conclude that there is a stronger, more pronounced diurnal cycle with a larger difference between the daily maximum and minimum mean rates during the summer compared to other seasons.

Analysis of the diurnal cycle based on the Integrated Multi-satellitE Retrievals for GPM (IMERG) data set also broadly support the presence of a late morning or early afternoon minimum and a maximum in the early morning hours over the Southern Ocean, and for the region near Macquarie Island (Tan et al., 2019; Watters & Battaglia, 2019). However, there are significant sampling and intercalibration challenges which are a major concern for the GPM products in this region (Tan et al., 2019). On a zonal basis, GPM radar and blended radar-plus-microwave data sets appear to substantially underestimate the annual mean precipitation rate as compared to CloudSat (Skofronick-Jackson et al., 2017; their Figure 5b), with zonal mean rates for GPM below 2 mm/day at 55°S, as compared to the approximately 2.9 mm/day (0.12 mm/hr) average from the Macquarie Island tipping bucket for the past 15 years. Much of this difference is likely due to the limited sensitivity to light precipitation of the GPM radar and associated microwave data. This is potentially problematic given the importance of light precipitation to the diurnal cycle and overall accumulation.

5. Modulation of Surface Precipitation Properties by Synoptic Conditions

How do precipitation characteristics vary by the synoptic setting? To investigate this in a simple way, we implement a quadrant method similar to Lang et al. (2018). The MICRE surface precipitation characteristics over 6 hr are sorted according to the position of the nearest low-pressure system. The situation is described as "far" in the event that no low-pressure center falls within 15° of the island (additional details in Section 2). The distribution of synoptic categories for each season is shown in Figure 5. This contains all times (not just those with good surface precipitation data). Restricting the plot to periods with good data makes no significant difference. The "far" category occurs most frequently in all seasons, followed by NE and NW, since low-pressure centers tend to pass to the south of Macquarie Island (Lang et al., 2018).

Figures 6 and 7 show the frequency of occurrence and the relative contribution by synoptic category to total accumulation, respectively. The frequency of small particle precipitation in Figure 6 varies little with synoptic category compared to rain and ice/mixed phase and occurs about 40% of the time. As discussed earlier, small particle precipitation most often comes from shallow clouds (<3 km). More interestingly, Figure 6 shows that

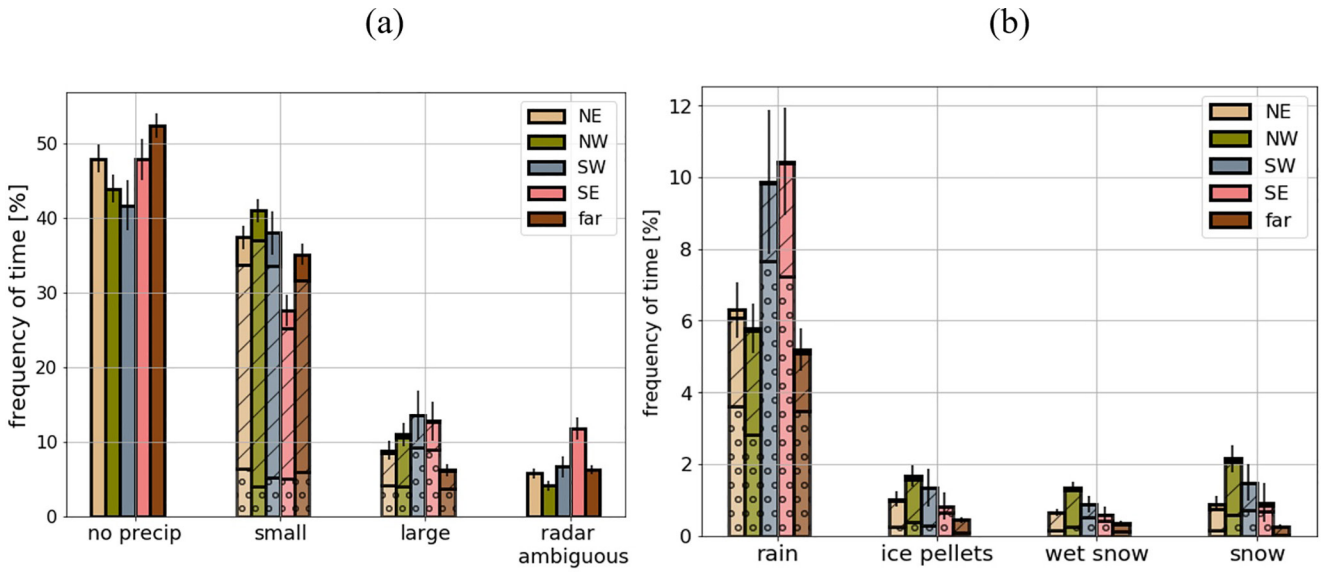

Figure 6. (a) Frequency of occurrence (percent of the time) of small particle, large particle and ambiguous precipitation. (b) Large particle precipitation broken into phase categories. For precipitating categories, solid colors indicate the fraction where no precipitation depth was retrieved due to missing radar data; dotted bars = deep (>3,000 m); cross hatched bars = shallow (<3,000 m).

rain occurs in all synoptic categories, but is most frequent when Macquarie Island falls in the SE quadrant, and is more often deep (extends above 3 km) in the SE and SW sectors compared to other categories. The largest mean precipitation rate (given by total accumulation in mm divided by total hours spent in each category) also occurs in the SE sector (Table 3), such that SE rain comprises about a third of the total accumulation (Figure 7, gray bar). The "far" category, on the other hand, has the lowest mean precipitation rate (Table 3) but occurs frequently (Figure 6a), and nonetheless contributes 11% to the total accumulation (Figure 7).

Regarding ice and mixed phase precipitation, the NW sector contains the most frequent occurrence of ice pellets, snow, and wet snow, and is responsible for much of the shallow depth (<3 km) ice and mixed phase precipitation. Surface temperatures reach their minimum values and are lower on average in the postcold front NW sector compared to other sectors, which is the case in all seasons (not shown). The occurrence of deep ice and mixed phase precipitation (>3 km), on the other hand, exceeds that of shallow in the SE. The highest clouds produced in SO cyclones have been observed to occur directly east of the low, with a southward extension due to clockwise rotation (Naud et al., 2014). While the precipitation in any quadrant is not necessarily due to a front, all synoptic categories show more frequent large particle precipitation than the "far" category. The large accumulation and rates in the SE quadrant seen in Figure 7 are consistent with advection of moist, warm air into the SE quadrant

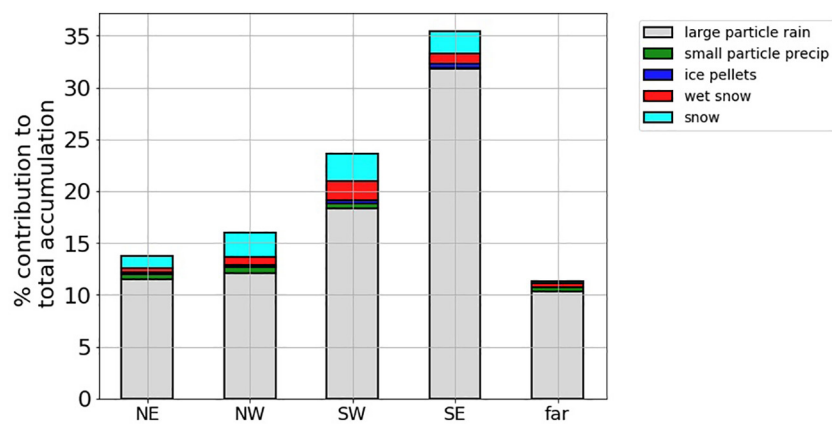

Figure 7. Contributions of each precipitation phase to total accumulated liquid by synoptic category.

Table 3
Average Blend Precipitation Rates, Tipping Bucket Rates, and Percent of Good Data by Synoptic Category

Synoptic category	Blend mean rates ± sampling uncertainty (mm/hr)	TB rates ± sampling uncertainty (mm/hr)	% Good blend data
NE	0.143 ± 0.042	0.129 ± 0.015	77%
NW	0.146 ± 0.038	0.145 ± 0.022	76%
SW	0.202 ± 0.070	0.173 ± 0.041	78%
SE	0.317 ± 0.089	0.254 ± 0.044	83%
Far	0.107 ± 0.028	0.100 ± 0.014	83%

via a warm conveyor belt (Field & Wood, 2007). The warm conveyor belt lofts moist air above the warm front, producing both heavy rain and deep ice/mixed phase precipitation in the SE. The contributions of ice and mixed phase precipitation to overall accumulation are largest in the SW and SE quadrants, reaching around 5% (Figure 7). Colder air in the postcold front conditions of the SW and NW quadrants results in more ice and mixed phase precipitation associated with shallow clouds.

We investigate the seasonal nature of ice and mixed phase precipitation and their dependence on surface temperature in Figures 8 and 9, respectively. Figure 8 shows the relative frequency of ice and mixed phase events by synoptic category and season. Figure 8 shows that ice and mixed phase events occur most often in winter when surface temperatures measured at the Macquarie Island station are coldest on average, regardless of the synoptic category. Although surface temperatures are lower on average during winter, the annual temperature variability at the surface is very small at Macquarie Island. Surface temperatures in Figure 9 are from the weather station at the Macquarie Island site. Figure 9 shows the frequency of occurrence of all precipitation types, binned according to the surface air temperature. For temperatures less than 2°C, large particle precipitation is dominated by ice and mixed phase precipitation (sum of blue, red and cyan bars), while for temperatures above 4°C, large particle precipitation is more often rain.

It is perhaps surprising to see in Figure 9 that glaciated precipitation occurs at surface temperatures exceeding 6°C. We stress that this is a log plot, and ice pellets, wet snow and snow account for 5% of all precipitation in the 6–8°C temperature bin. In the 0–2°C temperature bin, for comparison, ice pellets, wet snow and snow make up 18% of precipitation. While some of the glaciated events (especially snow classifications) are likely errors due to wind-induced artifacts that cause the false appearance of larger particles with low fall speeds, we have manually examined several events in detail to ascertain that at least some warm surface temperatures do indeed contain frozen precipitation. In general, frozen marine precipitation may reach the surface at temperatures well above 0°C. Using 3-hourly shipborne weather reports, Dai (2008) notes that over 5% of ocean snowfall was observed to occur at surface temperatures (~1.5 m above the ocean) of 5.5°C. Sims and Liu (2015) suggest that partially melted snow may occur more frequently in marine environments than over land because marine locations tend to have higher vertical lapse rates and higher relative humidity, leaving less time for falling snow to melt. Sounding data from Macquarie Island frequently show a weakly decoupled boundary layer with a moist subcloud "buffer layer" (Hande et al., 2012), whose existence we speculate has much to do with stabilization by evaporation of precipitation. Melting of frozen/mixed precipitation may also impact boundary layer dynamics by providing instantaneous cooling in below-cloud downdrafts and forming cold pools at the decoupled surface (Lang et al., 2021).

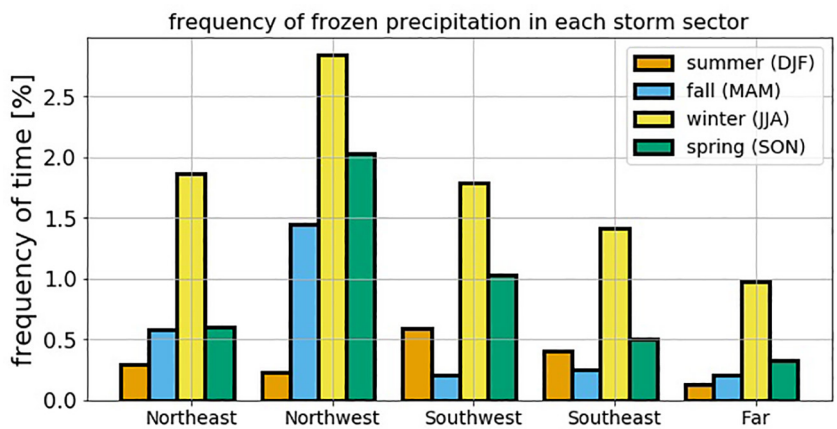

Figure 8. Frequency of ice and mixed phase events by synoptic category and season. The total frequency is normalized by total amount of time spent in each synoptic category (e.g., NE quadrant counts are normalized by the total number of 5-min Macquarie Island Cloud and Radiation Experiment (MICRE) blend points in the NE quadrant).

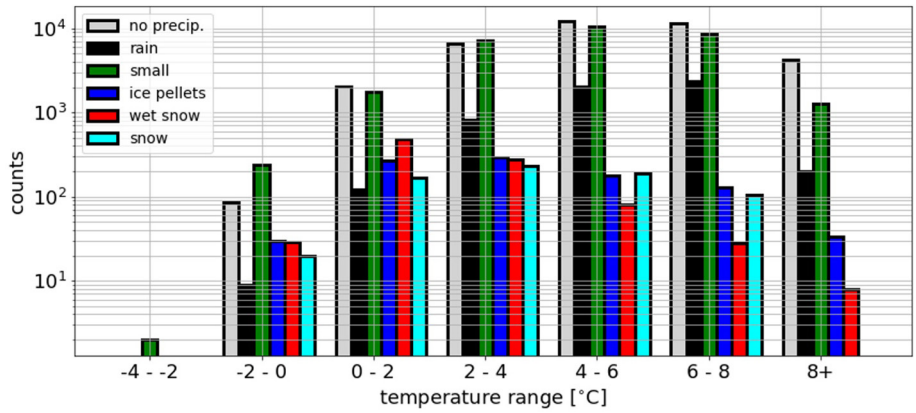

Figure 9. Histogram of each type of precipitation binned by temperature. Counts indicate precipitation data points of the Macquarie Island Cloud and Radiation Experiment (MICRE) blend data set.

6. Ground-Based Comparison to CloudSat

This section compares ground-based MICRE blend outputs with three operational CloudSat products: 2C-Precip-Column, 2C-Snow-Profile, and 2C-Rain-Profile (described in Section 2). We compare the MICRE data with CloudSat data using CloudSat data for both the period April 2016 to March 2017 and the full CloudSat record that was available to us at the start of the analysis, August 2006 to December 2017. We do this in part because CloudSat's narrow "curtain swath" results in a relatively low number of overpasses when examining only 1 year of data (see Supporting Information S1 for values by year and season). Some differences between the CloudSat data in 2016–2017 and from 2006 to 2017 should be expected because of differences in both space and time scales over which data are gathered, and in particular the summer of 2016 had larger accumulation than most other years (more on this later). We initially examined CloudSat data in a 10° latitude-by-10° longitude box centered on the island and broke this down into nine equally sized regions (3.3° per side), comparing results in each subregion. We found no significant longitudinal dependence in the CloudSat data over the 10° longitude box (results shown in the Supporting Information S1), though of course variations in precipitation characteristics do exist across larger longitudinal scales (Manton et al., 2020). We discuss the representativeness of the data to the broader SO in Section 7. We did, however, observe a strong latitudinal dependence in the CloudSat retrievals and again details of the analysis are presented in the Supporting Information S1. Consequently, the results shown in this section are limited to a 3.3° latitudinal band, centered on the island.

As described in more detail in Section 2.3, precipitation type (liquid, snow, mixed) is determined in the CloudSat 2C-Precip algorithm. For liquid precipitation, the confidence or likelihood is further categorized as certain, probable or possible, whereas for snow and mixed it is only certain or possible. Figure 10 compares the frequency of occurrence of liquid and frozen (ice/mixed) precipitation types. Here bars are broken into different colors to denote the associated CloudSat confidence category, or in the case of the MICRE blend data, to denote small and large precipitation particles or ambiguous radar detections. The CloudSat bars are based on the full record, with the thin black lines showing the combined sampling uncertainty. The overlaid blue star and thin blue lines show the 2016–2017 mean and estimated 1-sigma uncertainty. Overall, CloudSat indicates no precipitation about 68% of the time, while the MICRE blend indicates that precipitation is not present only 48–54% of the time, depending on the degree to which radar ambiguous periods (i.e., fog) are in fact precipitating. The disagreement in the frequency of nonprecipitating periods is largely attributable to situations where the surface ceilometer and radar indicate that below-cloud precipitation is present, but the reflectivity is less than −15 dBZ at 750 m to 1 km above the surface (the altitude range used by 2C-Precip in identifying precipitation type). Perhaps more striking are the differences in the categorization of precipitation phase. CloudSat has a much larger occurrence of ice or mixed precipitation, much of which is classified as being mixed phase with an estimated melt fraction between 0.1 and 0.9 (gray bar). This is problematic as neither 2C-Precip nor 2C-Snow provides a precipitation rate estimate for mixed phase precipitation when the melt fraction is between 0.1 and 0.9. Furthermore, the precipitation rate field in 2C-Snow is simply set to 0 for mixed phase with a melt fraction above 0.1. Consequently, users who do not carefully examine the data flags are unlikely to realize this contribution is missing.

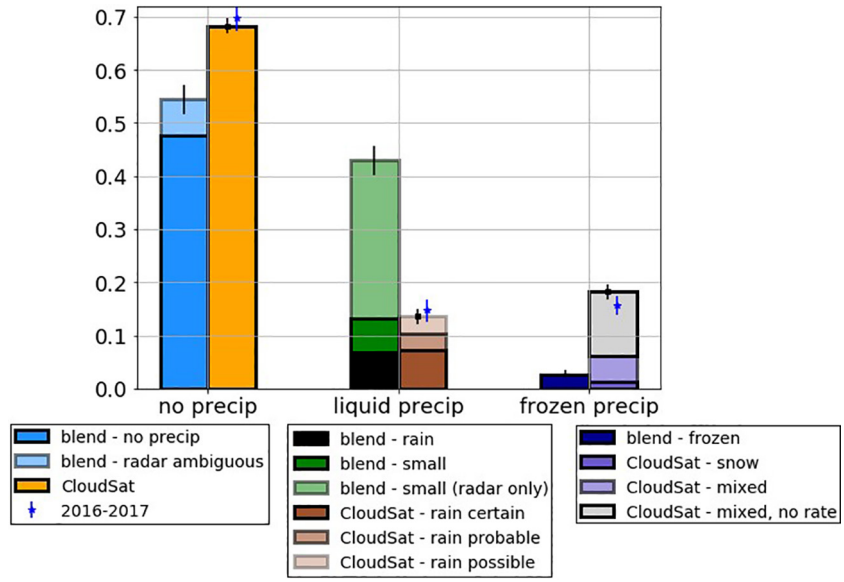

Figure 10. 2C-Precip phase-specific precipitation frequencies near Macquarie Island in comparison to the Macquarie Island Cloud and Radiation Experiment (MICRE) blend. Colored bars show CloudSat data from 2006 to 2017 (2,226 overpasses total) with black lines at the top of each colored bar showing the sampling uncertainty (defined as the standard deviation divided by the square root of overpasses for CloudSat and number of days for MICRE). Blue stars and vertical lines show means and uncertainty for CloudSat for the coincident period (2016–2017).

The overestimate in mixed phase precipitation is not surprising given that the CloudSat phase determination is largely driven by ECMWF temperature profiles; much of the low cloud covering the Southern Ocean is supercooled with cloud top-temperatures below freezing. The mean ECMWF reanalysis freezing level and mean MICRE radar melting layer both occur close to the surface, at 743 m (ECMWF) and 752 m (MICRE). Here, the ECMWF average was calculated using ancillary data included in CloudSat data products; the MICRE melting layer heights were found by using the height gradient of the radar Doppler velocity, which reaches a maximum at the height where frozen hydrometeors melt and become denser.

While this comparison is statistical, it suggests that much of the small particle (low reflectivity) precipitation observed from the surface radar and ceilometer is going undetected by CloudSat or being categorized as mixed phase, when it is predominantly liquid. Figure 11 shows the distribution of below-cloud, near-surface reflectivity (meaning between 150 and 250 m above the surface) from the BASTA W-band radar for periods identified as (i) small particle precipitation-only, and (ii) all precipitation (small + large particle precipitation including rain, ice pellets, snow, wet snow). The distributions converge at low reflectivity values, indicating that reflectivity values below about −10 dBZ are dominated by small particle precipitation, while large particle precipitation (rain + ice + mixed) dominates the occurrence above 5 dBZ. Precipitation with a reflectivity below −15 dBZ, the identification threshold used by CloudSat, occurs about 17% of the time. This accounts for the difference (Figure 10) in fractions of CloudSat no precipitation versus MICRE no precipitation.

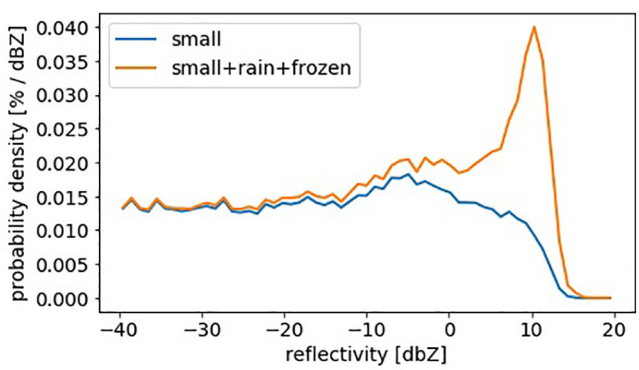

Figure 11. Distribution of near-surface reflectivity from the Bistatic rAdar SysTem for Atmospheric studies (BASTA) radar (mean reflectivity between 150 and 250 m). The blue line is for small particle precipitation, and the orange line is for small + large particle precipitation (rain, ice pellets, snow, wet snow).

We examine the CloudSat reflectivity data in more detail in Figure 12, where joint radar reflectivity-height histograms for the CloudSat precipitation categories are plotted. The precipitation categories are no precipitation, liquid, mixed phase and snow. Mixed phase is additionally separated into zero rate (melt fraction >0.1) and nonzero rate (melt fraction <0.1). We include the two separate mixed phase plots (Figures 12c and 12d) to distinguish between situations where the melt fraction was considered too large to provide a snowfall rate estimate versus where the melt fraction was sufficiently small and precipitation was treated as snow. Here the height bins are set to match

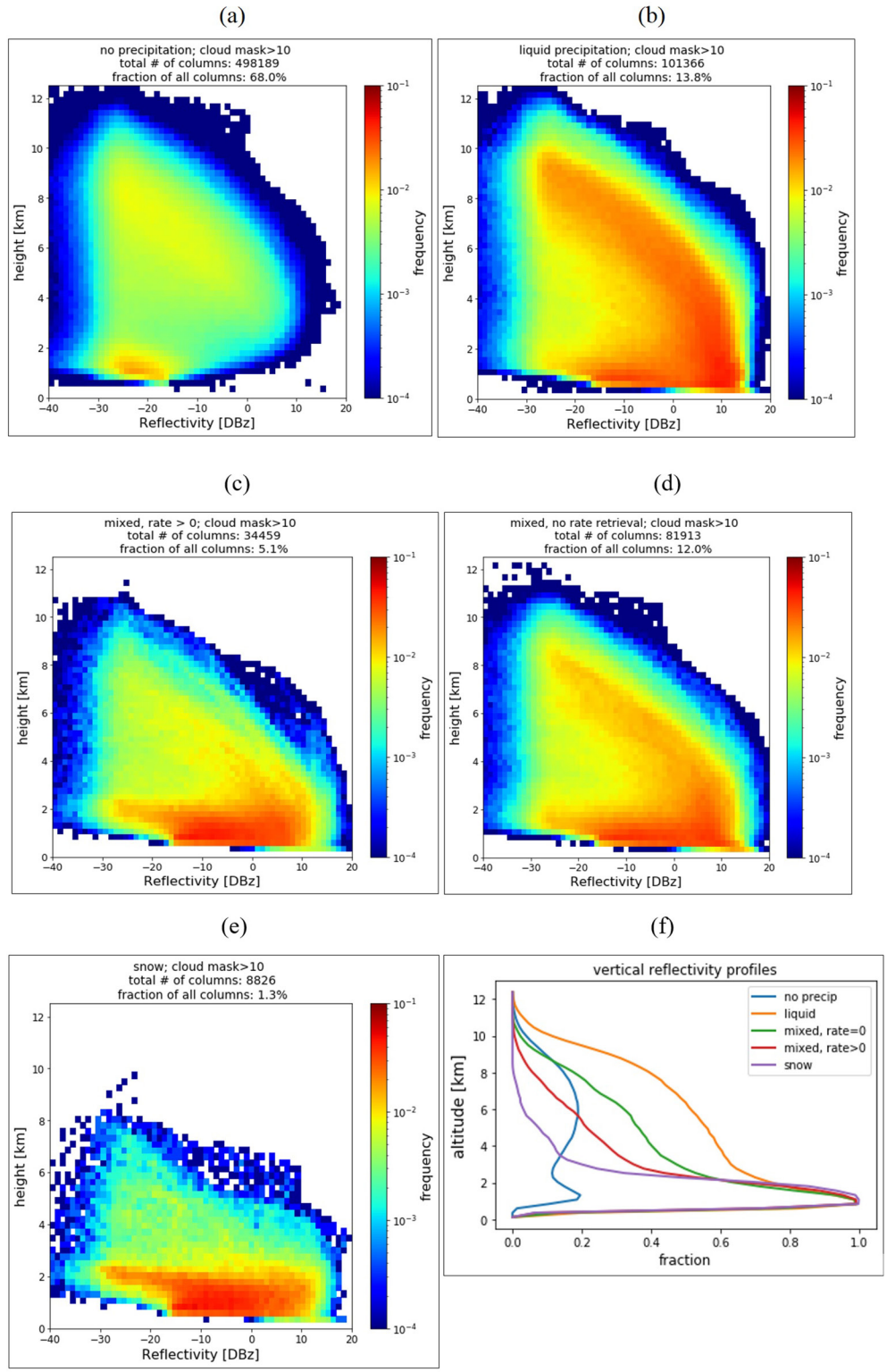

Figure 12. CloudSat radar reflectivity-height histograms for (a) no precip., (b) rain (certain, probable and possible), (c) mixed phase precip. with a nonzero rate retrieval in 2C-Snow (d) mixed phase precip. with no rate retrieval in 2C-Snow, and (e) snow (melt fraction = 0 and snowfall rate is >0 in 2C-Snow). Panel (f) shows the total reflectivity fraction as a height profile for panels (a–e).

the CloudSat vertical sampling of 240 m, and reflectivity bin widths are 1 dBZ. At the top of each histogram the total number of radar columns is given, along with the fraction of radar columns in each category. Figure 12f shows the total frequency of occurrence at each vertical level (obtained by summing the histogram across all reflectivity values).

The −15 dBZ threshold at 1 km, used to categorize events as precipitating or nonprecipitating, is evident in the CloudSat histograms, which show that reflectivity values at 1 km are almost always larger than −15 dBZ in the precipitating categories (Figures 12b–12d and 12e). For nonprecipitating clouds (Figure 12a), the reflectivity at 1 km is usually <−15 dBZ. Note the colors depicting the histogram frequency of occurrence are on a logarithmic scale, and the frequency of occurrence in each plot is normalized by the total number of CloudSat columns in the category plotted. This is done to emphasize the relative contribution of differing reflectivity values within each category, and to obtain in-category occurrence profiles (Figure 12f). Histograms in all categories show a relatively low occurrence of reflectivity values below about −30 dBZ as compared with above −30 dBZ. This is because the CloudSat sensitivity limit (or the noise floor, more precisely) is close to −30 dBZ and the radar does not reliably detect hydrometeors near/below the noise floor (Marchand et al., 2008; Tanelli et al., 2008). These plots therefore should not be interpreted to mean that hydrometeors rarely have reflectivities below −30 dBZ. Surface clutter likewise increasingly limits detection of hydrometeors below about 1 km such that only strong reflectivity signals (>5 dBZ) can be detected in the height bin from 250 to 500 m above the surface (Marchand et al., 2008).

The effect of clutter is especially evident in Figure 12f, which shows the CloudSat vertical profile of hydrometeor occurrence in each precipitation category, obtained by summing each histogram across all reflectivity values. For the rain, snow, and mixed phased categories, a "peak" frequency near one is evident at 1 km. The frequency of occurrence below 1 km does not remain near one because the reflectivity due to precipitation drops below what can be detected above the clutter; it is not due to evaporation. The reduction above 2 km, on the other hand, is due to a reduction in the presence of precipitation and shows that much of the precipitation in all of these categories is coming from shallow clouds, consistent with the analysis of the MICRE surface data in Section 3 (Figure 2). This is especially true for CloudSat precipitation identified as snow with an estimated melt fraction of zero. The mixed phase histograms (Figures 12c and 12d) also show that much mixed precipitation is coming from shallow clouds, but have a higher occurrence of hydrometeors above 2 km, indicating deeper precipitation formation (some of the time) in comparison to snow. Mixed phase with no rate retrieval (Figure 12d) contains deeper systems on average, and occurs more frequently (12% of the time), suggesting that a nontrivial contribution to the total annual precipitation is missing.

Table 4 lists total seasonal and annual accumulations from the MICRE blend, tipping bucket, and CloudSat products. Here the accumulations are calculated based on the seasonally averaged precipitation rates, which include nonprecipitating periods (rate = 0 mm/hr), multiplied by the number of hours of good data in each season. The top value given in tipping bucket/CloudSat cells is the value for the MICRE period (March 2016 to February 2017). For the tipping bucket and CloudSat products the second and third numbers given are the mean and standard deviations (in parentheses) for the 11-year period, 2006 to 2016. Mean precipitation rates in individual seasons and years can be found in the tables in the Supporting Information S1. The total accumulation (rain + ice + mixed + small) based on the MICRE blended surface data is about 1,423 mm, which is slightly larger than that from the tipping bucket alone because of the contribution of radar only detected light precipitation.

The coincident 2C-Precip average accumulation (1,533 mm) is larger than both the tipping bucket and the blend accumulations despite the fact that the 2C-Precip data (i) does not include contributions by ice or mixed phase, and (ii) is missing the contribution of precipitation with near-surface reflectivity <−15 dBZ. We note that the MICRE period, especially the summer (DJF), was exceptionally wet according to the tipping bucket. For the MICRE DJF period (starting in December 2016) the tipping bucket accumulation is 458 mm compared to a mean of 288 mm from 2006 to 2016, and the annual accumulation for the MICRE period is 1,351 mm as compared to an annual mean of 1,068 mm over the past 11 year. But the 2C-Precip data does not show 2016 to be unusually wet (DJF in 2016 was 392 mm versus an 11-year mean of 499 mm, and annually 1,533 mm in 2016 versus an 11-year mean of 1,537 mm). In Section 7, we discuss the implications of MICRE being an unusually wet period, but regarding the evaluation of CloudSat, the more immediate point is that the CloudSat 2C-Precip product overestimates the total surface precipitation. Over the 11-year period of the CloudSat data record (2006–2016), the ∼1,500 mm of average annual precipitation estimated by CloudSat is larger than any year in the tipping bucket

Table 4
Seasonal and Annual Accumulations From Blend, Tipping Bucket, and CloudSat Products

Season 2016 Mean 2006–2016 (Std 2006–2016)	Blend ice/ mixed (mm)	Blend small (mm)	Blend rain (mm)	Blend total (mm)	Tipping bucket (mm)	2C-Precip (mm)	2C-Rain (mm)	2C-snow (mm])
Fall (MAM)	64.0	39.0	239.2	342.2	331.5	450.2	242.6	9.3
					287.2	**425.7**	**196.4**	
					(40.8)	(173.5)	(109.4)	
Winter (JJA)	58.4	54.4	251.7	364.5	310.0	342.9	187.2	53.5
					233.6	300.6	**122.2**	
					(51.6)	(182.8)	(130.6)	
Spring (SON)	31.6	34.3	229.1	295.0	251.5	348.2	88.4	43.0
					259.3	257.3	**96.9**	
					(41.1)	(177.9)	(98.5)	
Summer (DJF)	36.3	21.2	363.7	421.2	457.6	391.5	91.7	2.8
					287.5	**498.5**	259.5	
					(80.7)	(311.0)	(226.7)	
Annual	190.3	148.9	1083.7	1422.9	1350.9	1532.8	610.0	108.6
					1067.6	**1537.0**	**697.9**	
					(123.2)	(355.8)	(366.2)	

Note. The top number in each cell is the value for the MICRE period (April 2016 to March 2017). For Tipping Bucket and CloudSat, the middle numbers are the mean accumulation for 2006–2016 and the bottom number in parentheses is the standard deviation across 2006–2016. Bold values indicate CloudSat 11-Year means that are biased high or low based on a statistical *t* test. The 2C-Precip data includes all confidence levels (rain certain, probable & possible).

record. The tipping bucket average is less than 1,100 mm for the same 11-year period. The >400 mm difference between 2C-Precip and tipping bucket annual means cannot be explained as a result of additional accumulation from light precipitation that is missed by the tipping bucket (unless the accumulation due to light precipitation that is missed by the tipping bucket is much larger in most years than the ∼150 mm we estimate during MICRE from the radar). Applying a statistical *t* test (e.g., von Storch & Zwiers, 2002, Section 6.6.4) for the difference in the means indicates that the CloudSat 2C-Precip annual mean precipitation during the 2006–2016 period is (at the 95% level of confidence) too large relative to the tipping bucket. Periods during which the CloudSat mean accumulation are biased at the 95% confidence level are shown in bold in Table 4, and include the 2C-Precip estimated surface accumulation for MAM and DJF.

2C-Rain, on the other hand, has the opposite problem and underestimates the total annual accumulation. To some degree this should be expected because 2C-Rain includes only radar columns flagged as "rain certain," but as will be shown in more detail below, the problem is systematic and much larger than missing contributions from lighter and less certain rain.

Lastly, 2C-Snow accumulations appear to be lower than the MICRE ice + mixed phase accumulation, due predominantly to underestimates during summer and fall. This is presumably due to a lack of mixed phase retrievals when melt fractions are between 0.1 and 0.9, but there is a complex cancelation of errors happening here: columns are flagged as mixed phase too frequently, but many are missing precipitation rate retrievals.

Regarding the variability, CloudSat is a nadir-only pointing instrument and only infrequently samples the region near Macquarie Island. The number of times each year that CloudSat passed within 10 degree of Macquarie Island and had a good retrieval is given in the Supporting Information S1. The effect of the infrequent CloudSat sampling on accumulation is large. Notice that the standard deviations in seasonal and annual accumulation in Table 4 are about a factor of 3 larger for CloudSat than for the tipping bucket. The correlation coefficient between the 2C-Precip and tipping bucket annual accumulation (annual values are again given in Supporting Information S1) for the 2006–2016 period is about −0.1, meaning there is essentially no correlation. We show in the Supporting Information S1 (Section S5) that this low value for the correlation is largely a result of chance, and if

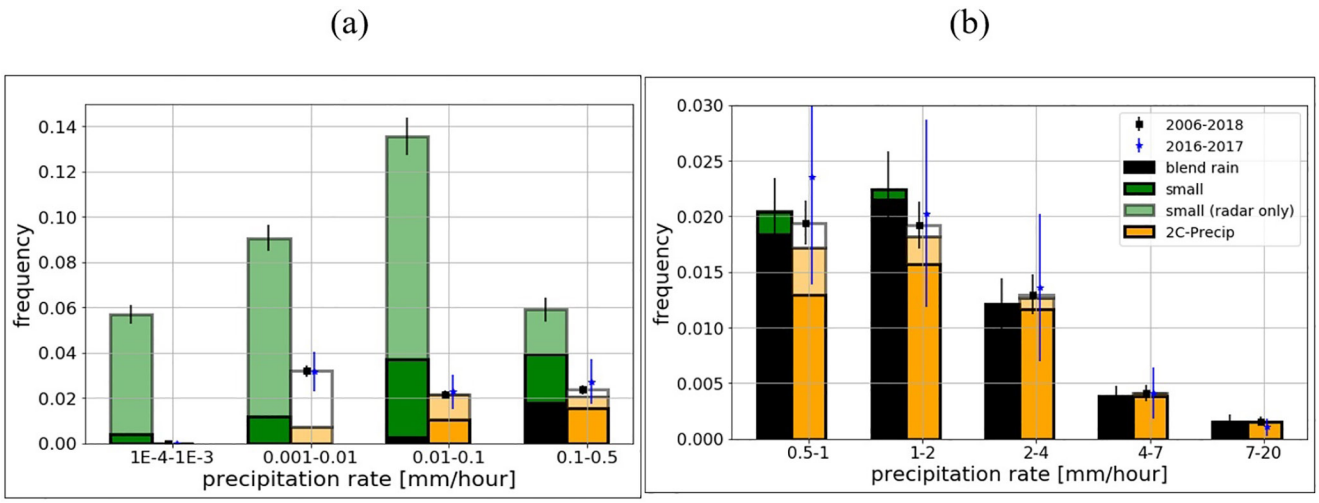

Figure 13. 2C-Precip and blend frequencies at (a) light rain rates and (b) moderate to heavy rain rates. Vertical axis gives the fraction of time that it rains at the rate specified. Black lines at the top of each colored bar show the sampling uncertainty, while blue stars and blue lines denote the CloudSat 2016–2017 (Macquarie Island Cloud and Radiation Experiment (MICRE) coincident period) mean and estimated sampling uncertainty. Black bars = blend rain (large particles). Dark green = blend drizzle (small particles) detected by both radar and disdrometer. Light green = blend drizzle (small particles) detected by radar only. Orange bars are CloudSat 2006–2017 averages, with dark orange bars = "rain certain," light orange = "rain probable," and white = "rain possible".

one shifts the CloudSat sampling time by 1 day or a few days, one can obtain a correlation coefficient that varies anywhere between about 0 and 0.6 only due to sampling. At a practical level the infrequent CloudSat sampling makes it difficult to use CloudSat for the study of annual or seasonal variability for any specific surface site.

In Figure 13, we compare CloudSat 2C-Precip (single column, ~2 km field of view) rain rates with the MICRE blend product 5-min rates, broken into two panels for (a) light rain rates and (b) moderate to heavy rain rates. The MICRE occurrence of all rain rates (black and green bars in Figure 13) sum to 40%, which is lower than the ~43% given in Figure 10 for liquid precipitation. This is because about 3% of the time, near-surface, below-cloud precipitation is present (radar shows hydrometers are present) but the precipitation is too light for the surface disdrometer (typically this means a rain rate less than 0.5 mm/hr), and the radar retrieval either failed to estimate the rain rate or the estimated radar rain rate is less than 10^{-4} mm/hr. Typically, the radar retrieval fails because the algorithm is not able to extract with confidence the particle fall velocity from the total measured Doppler velocity. CloudSat retrievals are color coded to denote the confidence level (dark orange = "rain certain"; light orange = "rain probable"; white bars = "rain possible"). Most of the CloudSat retrievals are categorized as certain, meaning the near-surface (attenuation corrected) reflectivity is larger than 0 dBZ and it is very likely precipitating at the surface. This includes most but not all of the precipitation with a rain rate larger than 0.5 mm/hr. Black and blue vertical lines at the top of each bar show the sampling uncertainty (given by the standard deviation divided by the square root of the number of overpasses). The black lines are for the full data record and blue the coincident 2016–2017 period). Not surprisingly, sampling uncertainty based only on the coincident data is much larger than the 11 years average. However, regardless of using the coincident or full data record uncertainties, it is clear that the MICRE data show a higher occurrence at rain rates below 0.5 mm/hr. Consistent with the discussion of Figures 10 and 11, most of this precipitation is composed of small particles with relatively small reflectivities. The difficulty with light precipitation aside, the distribution of rain rates in 2C-Precip compares reasonably well against the blend data rain rates that contain larger particles, with the CloudSat values generally matching the MICRE values to well within the sampling uncertainty of both the coincident period and full record.

For precipitation identified as snow/mixed phase, CloudSat 2C-Snow provides an estimate for the precipitation rate, but only when the estimated melt fraction is less than 0.1. Figure 14 compares ice/mixed precipitation rates from 2C-Snow and MICRE. The MICRE data shows few events with precipitation rates larger than 2 mm/hr. As discussed previously, much of the ice/mixed precipitation appears to be light and associated with shallow clouds. Overall, CloudSat appears to overestimate the frequency of ice/mixed precipitation compared to MICRE, even when restricted to melt fractions less than 0.1. However, the MICRE data only identifies ice/mixed precipitation

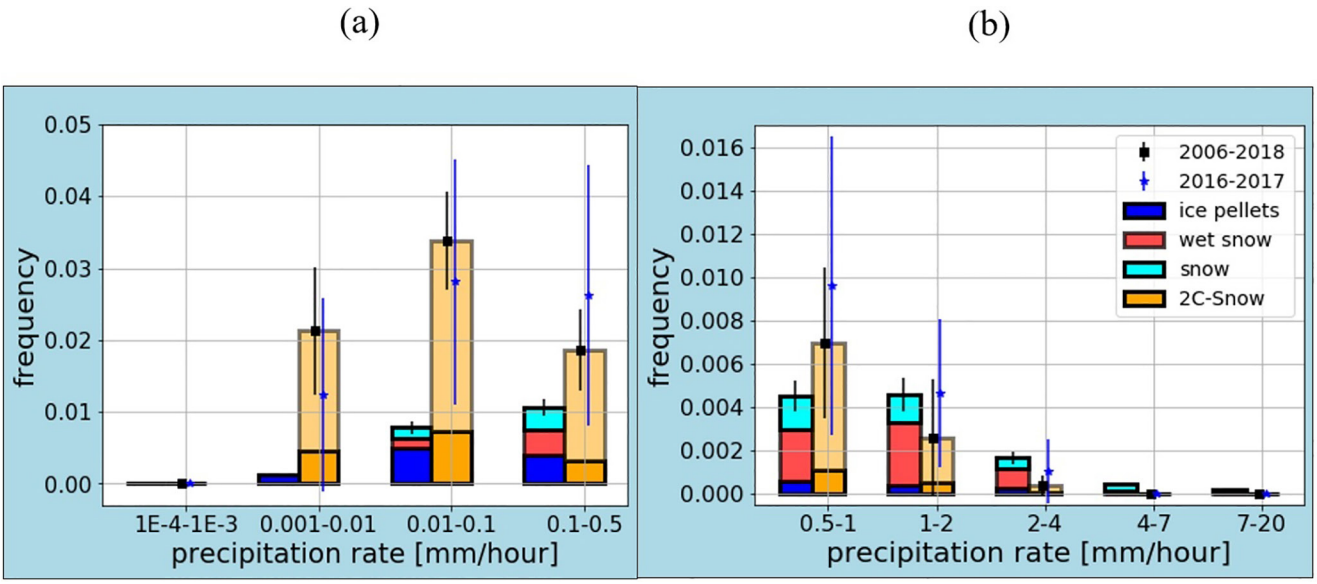

Figure 14. As Figure 13 except for 2C-Snow-Profile and ice, snow, and wet snow surface precipitation types.

unambiguously when the precipitation particle size is large, and some of the small particle precipitation is likely frozen.

As described in Section 2, the CloudSat operational product 2C-Rain-Profile provides a vertical profile of rain rates for radar columns previously flagged as containing rain (liquid phase precipitation) in the 2C-Precip retrieval. 2C-Rain provides rain rates solely for the columns defined as "rain certain," meaning columns with an attenuation corrected near-surface reflectivity >0 dBZ. The 2C-Precip and 2C-Rain rain rates near the surface are not the same. The algorithms make different assumptions regarding the precipitation particle size distribution, and 2C-Rain includes a treatment for below-cloud evaporation, which is not treated in 2C-Precip. Similar to Figures 13, Figure 15 compares 2C-Rain rain rates with the MICRE blend. (The MICRE data in Figures 13 and 15 are the same.) The distribution of rain rates shown in 2C-Rain is bifurcated with one peak between 0.01 and 0.1 mm/hr (Figure 15a) and the other between 2 and 4 mm/hr (Figure 15b). While in some sense 2C-Rain better captures the presence of light rain rates than 2C-Precip, it is doing so at the expense of heavier rates whose occurrence is substantially underestimated. This is to some extent because the effect of evaporation is too large in

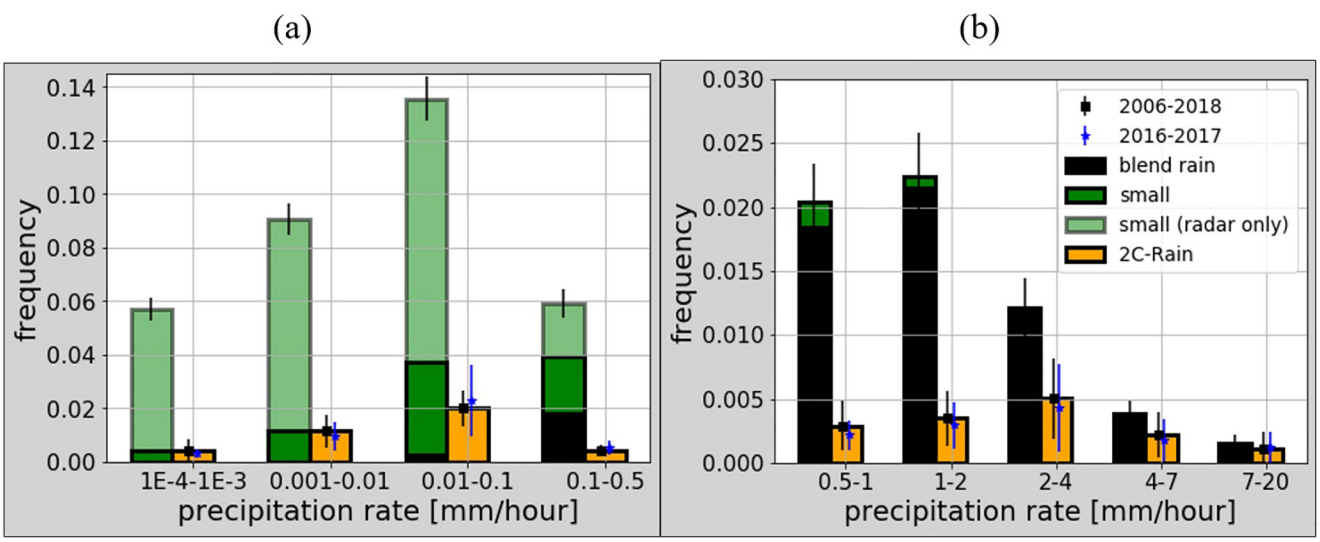

Figure 15. As in Figure 13, except for CloudSat 2C-Rain product. 2C-Rain product includes rain rate estimates only for rain certain events.

2C-Rain. Of the rain certain columns, 2C-Rain estimates that the evaporation percentage equals 100% (meaning 2C-Rain contains a rain rate of zero) about 21% of the time. While most of the fully evaporated columns have 2C-Precip rates that are less than 0.1 mm/hr, a nontrivial number of 100% evaporated cases have a 2C-Precip rate that is 0.5 mm/hr or larger. The 2C-Rain product stores the estimated evaporated rain fraction for each radar column. As an experiment (not shown), we have artificially restored the evaporated fraction to the 2C-Rain rain rates for those columns that were not 100% evaporated. The comparison indicates that even with evaporated rain added back in, however, the 2C-Rain product substantially underestimates occurrence of rain rates between 0.5 and 2 mm/hr compared to 2C-Precip. Thus, we conclude that excess evaporation is not the only problem in 2C-Rain, and we speculate that the assumed precipitation drop size distribution (DSD) likely contains too few drops larger than 0.5 mm. The 2C-Precip algorithm assumes an exponential DSD with fixed intercept parameter (Marshall & Palmer, 1948), while the 2C-Rain algorithm on the other hand assumes an exponential DSD with a parameterization of the intercept parameter dependent on the rain water content, such that rain rate and intercept parameter are anticorrelated (Abel & Boutle, 2012). As part of future work, the MICRE disdrometer data should allow us to test the fidelity of these parameterizations.

As is, 2C-Precip surface rain rates should probably be used in preference to those from 2C-Rain with respect to total accumulated precipitation over the SO, but with the understanding that the total liquid phase accumulation in 2C-Precip is too large, light liquid precipitation is under-represented (in frequency and amount), and the presence of mixed phase is over-represented in frequency (although most of it has no associated precipitation rate in 2C-Snow). That is, there is a large cancelation of error with the overestimate in total accumulation in 2C-Precip liquid precipitation being balanced by missing contributions from mixed phase precipitation. It should be emphasized that this suggestion is specific to this region of the SO and in general there is strong latitudinal dependence on the precipitation phase in the CloudSat retrievals (see also Supporting Information S1). In particular, it has been shown that the 2C-Precip rates substantially overestimate surface rates in subtropical stratocumulus regimes (Bretherton et al., 2010).

7. Discussion

As mentioned at several points in the manuscript, the MICRE blended surface precipitation data set covers a period that is just under 1 year in duration and consequently, these data do not characterize interannual or longer timescale variability. In particular, the given sampling uncertainties are indicative of how well we know a given value for the observational period given day-to-day variability but not year-to-year or longer timescale variability. So, for example, we find that in fall, winter and spring the frequency of small particle precipitation was 34–47% during MICRE. This does not mean that the frequency of small particle precipitation will fall between 34% and 47% in these seasons every year (or to be more precise, 68% of years since the uncertainties shown are the estimated 1-sigma uncertainty), because for example, longer timescale variability in synoptic activity associated with the Southern Annular Model might act to increase or decrease the occurrence in any given year. Rather, what the estimated sampling uncertainty does is inform us that the small differences in this frequency for fall, winter and spring (shown in Figure 2) are not meaningful (the differences are within what one expects given a ∼90 days sample and the observed level of day-to-day variability). But the much larger difference in the occurrence of small particle precipitation in summer (at 19%) is unlikely to be a result of the day-to-day variability and the finite length of the observations. While we cannot eliminate the possibility that the large difference between summer and other seasons in the frequency of small particle precipitation shown here is a result of interannual variability, in our judgment it is unlikely that all or most of the difference is due to interannual variability. The same holds true for all of the key points itemized in the concluding section (that follows this discussion).

One facet where consideration of interannual variability is of particular importance is accumulation. For MICRE, the total accumulation during the summer was larger than the other seasons. However, the long-term tipping bucket record at Macquarie Island indicates peak precipitation occurs in the fall, not summer, with March having the greatest accumulation (Wang et al., 2015). In relation to the longer-term tipping bucket record at Macquarie Island, the MICRE summer months (December 2016, January and February 2017) have the highest total accumulation within the period 2002–2016, and relative to the record going back to 1970, one can characterize the MICRE summer period as an outlier (more than a 2-sigma event).

However, precipitation is changing in the region. Adams (2009) reports that over the period 1970–2008, winter precipitation at Macquarie Island increased by 55%, fall by 20%, summer by 9% and spring by 28%, with average annual precipitation increasing from 800 mm to around 1,080 mm. More recently, Manton et al. (2020; Figure 5) show a strong trend in summer precipitation (larger than any other season) at Macquarie Island due to high values in recent years. To be clear, Manton and coauthors view the high summer values as outliers; and we do not dispute that, relative to the long record (the current baseline), this is true. Our point is rather that 30 years from now, the larger values observed in recent years at Macquarie Island may not be unusual. Regardless of whether or not one defines the MICRE summer as an outlier, we stress that there is significant interannual variability in accumulation and one should not take the seasonal accumulations (and differences in accumulation between the seasons) observed during MICRE to be indicative of the climatological mean.

Another important topic is the relationship between the surface precipitation characteristics observed during MICRE to those of the SO. There are at least two aspects here. First, to what degree can the observations during MICRE be extrapolated to the broader SO? And second, how representative is the MICRE observations to the local region surrounding the island? Is there an "island effect"?

With respect to the broader SO, many studies have shown that there are significant longitudinal and latitudinal variations for both cloud properties (e.g., Huang et al., 2016) and mean precipitation rates (e.g., Manton et al., 2020, see maps from Hayden & Liu, 2018), and in any quantitative sense, one does not expect the mean precipitation rates and frequencies of occurrence to extend far from the island. This is especially true for the amount and frequency of snow and mixed phase precipitation. In the evaluation of CloudSat products presented in Section 6, we found little variation in CloudSat properties for longitudes within $\pm 5°$ of Macquarie, but a strong latitudinal stratification that required restricting the CloudSat data used in our comparison to a few degrees of latitude. Details of this analysis are given in the Supporting Information S1. The same sharp latitudinal transition in these precipitation types can also be seen in the geographical maps given by Behrangi et al. (2014; Figure 1).

But many of the general characteristics observed during MICRE are likely qualitatively similar. In particular, the high frequency of light precipitation and the small (but not trivial) contribution this makes to the total accumulation, the diurnal cycle (at least regarding the presence of a local minimum in the early afternoon), the presence of mixed phase precipitation coming from both shallow and deeper precipitation systems (with shallow mixed phase precipitation being more prevalent in the colder air to the NW of cyclonic lows), and the dependence of frozen/mixed phase precipitation on surface air temperature are all likely to be characteristic of the broader SO. While limited-duration ship and aircraft based measurements have not mapped out the seasonal variations to the degree done here, they certainly support the frequent occurrence of light precipitation and presence of mixed phase precipitation in shallow cloud systems (e.g., Mace et al., 2021; Mace & Protat, 2018a, 2018b; McFarquhar et al., 2021).

Another potential concern with the MICRE data is the possibility that the island might influence the atmospheric state and the observed cloud and precipitation properties. The measurement site is situated on a narrow isthmus near the north end of the island. There is an open fetch to the west (the predominant wind direction) but potentially significant orography exists to the south, with a peak elevation of 410 m. However, numerical simulations using the Weather Research and Forecasting (WRF) model with and without terrain by Wang et al. (2016) find that the overall orographic effects on the precipitation record are not significant, other than an enhancement of drizzle that can occur with southwesterly winds. About 20% of MICRE light precipitation (rates <0.1 mm/hr) occurred with south/southwesterly winds, and we cannot entirely discount that orographic effects have had an impact in these cases. As part of ongoing work on cloud properties observed during MICRE, we plan to investigate possible island effects using MODIS data and this may shed some additional light on the presence of island effects. Certainly, it is not rare to observe perturbations in the MODIS images of low altitude cloud fields downwind of the island.

A major focus of the present analysis has been on light precipitation in both the MICRE surface blend and CloudSat 2C-Precip data sets. As mentioned at several points in this study, some of the light precipitation identified in the MICRE blend product is likely virga that evaporates below 250 m. In most respects, CloudSat faces the same difficulty of having to use near-surface reflectivity observations to estimate surface precipitation, but must do so using observations collected even further above the surface (typically 0.75–1 km). Regardless of whether or not it is virga, it should be stressed that the existence of extensive light precipitation is likely important to aerosol

scavenging and cloud lifetime (Wood, 2006, 2012), as well as its effects on boundary layer stability, dynamics and thermodynamics due to evaporation. Broadly speaking, understanding how precipitation modifies cloud droplet concentrations and cloud albedo among other cloud properties is crucial to understanding energy fluxes related to low clouds (e.g., Savic-Jovcic & Stevens, 2008). Given the large occurrence of low clouds over the SO, it seems likely that models will have to represent light precipitation and associated precipitation-cloud-aerosol interactions well if they are to simulate SO energy fluxes and global climate cloud-feedbacks accurately. Silber et al. (2021) have also recently documented and emphasized the importance of extensive light precipitation from supercooled liquid clouds at McMurdo Station, Antarctica (78°S) and on the North Slope of Alaska (69°N), and in this sense the SO is not unique (although at those sites, the light precipitation appears to be ice more than supercooled drizzle). Nonetheless, this analysis suggests that continued efforts should be made to observe and study SO light precipitation characteristics and precipitation-cloud-aerosol interactions.

8. Summary

Previous studies have documented that SO clouds, including the wide-spread shallow (low altitude cloud top height) clouds that dominate total cloud cover, are frequently precipitating with liquid, frozen, and mixed phase precipitation (Ahn et al., 2017; Chubb et al., 2013; Lang et al., 2018, 2020; Mace & Protat, 2018a, 2018b; Wang et al., 2015). The primary addition that MICRE measurements and the present analysis provide to previous data sets and studies comes from having a year of W-band radar, ceilometer, and disdrometer measurements that allow an examination of seasonal, diurnal, and synoptic variations in surface precipitation type and particle size (in addition to accumulation), though interannual variability may impact each of these to varying degrees as discussed in the previous section. Key results are:

1. Precipitation dominated by small particles (and falling mostly at light rates that are difficult to capture with a tipping bucket) occurs much more frequently than precipitation composed of large particles
2. In fall, winter and spring, the total frequency of both large and small particle precipitation is similar, with small particle precipitation occurring 34–47% of the time and large particle precipitation occurring 7–12% of the time. Summer is markedly different from the other seasons in having much less small particle precipitation (occurring ∼19% of the time)
3. At Macquarie Island, liquid and ice/mixed surface precipitation occur in all seasons, with accumulated precipitation being due more to rain (large particle liquid precipitation) than drizzle (small particle precipitation) or ice/mixed precipitation
4. The contribution from small particle precipitation to accumulation is nonnegligible and constitutes ∼10% of the total annual precipitation
5. There is a statistically significant diurnal cycle in precipitation occurrence and mean surface precipitation rate with a daily minimum in the early afternoon between 12:00 LT and 14:00 LT
6. Surface precipitation containing large particles ($D > 1$ mm) is more likely to be glaciated (ice or mixed phase) when the surface air temperature is below 2°C, and more likely to be liquid above 4°C. During MICRE, glaciated surface precipitation accounted for about 5% of all precipitation (by frequency) above 6°C (see Figure 9)
7. Ice/mixed precipitation are frequently found coming from shallow precipitating systems (−15 dBZ echo top <3 km) and most often this happens when Macquarie Island is to the NW or SW of the nearest low-pressure center (likely in the postcold frontal region of baroclinic systems where mesoscale cellular convection occurs). Deeper ice/mixed precipitation systems (>3 km) contribute more to the total accumulation and occur most often when Macquarie Island is in the SE and SW quadrants
8. Not surprisingly, we find that the majority of small particle precipitation (which comprises most of the precipitation with rates below 0.5 mm/hr) is shallow (−15 dBZ echo top <3 km). Perhaps more surprising is that the frequency of occurrence of small particle precipitation is remarkably close to 40% in all synoptic categories. This includes the synoptic category "far," meaning no low-pressure center is within 15° of the island in latitude or longitude. While the "far" category has the lowest mean precipitation rate, it nonetheless comprises about 11% of the total annual accumulation
9. Large particle precipitation, on the other hand, has noteworthy variations between synoptic categories. Rain (large particle liquid precipitation) occurs in all synoptic categories, but (i) is most frequent and has the largest mean rain rate when Macquarie Island is located to the SE of the nearest low-pressure center, consistent

with Lang et al. (2018), and (ii) is more often deep (extends above 3 km) in the SE and SW categories than in the other synoptic categories. This is consistent with the structure of mature baroclinic systems and the presence of a warm conveyor belt (Field & Wood, 2007), and is consistent with composites of cloud and precipitation structures observed using CloudSat, Calipso and other satellite retrievals over the SO by Naud et al. (2014)

10. The operational CloudSat 2C-Precip-Column product (Release 05) overestimates the total liquid phase accumulation, under-represents the frequency of light liquid precipitation (rates <0.5 mm/hr), and overestimates the frequency of mixed phase precipitation (with most of the mixed phase precipitation having no associated precipitation rate in 2C-Snow-Profile or any other CloudSat operational product)
11. The CloudSat 2C-Rain-Profile product, on the other hand, substantially underestimates both the occurrence and amount of liquid precipitation, with significant underestimates in the occurrence of both light (<0.5 mm/hr) and heavy (>0.5 mm/hr) rain rates. Errors in 2C-Rain are due in part (but not in whole) to an overly strong modeling of evaporation

Data Availability Statement

CloudSat data are available via the CloudSat Data Processing center (https://www.cloudsat.cira.colostate.edu/). DOE program instrument level data (including Parsivel and ARM ceilometer data sets) are available through the DOE Atmospheric Radiation Measurement (ARM) program data archive (https://adc.arm.gov/). PIRAT and blended data products, as well as synoptic classification, radar, and tipping bucket data will be available from the ARM program principal investigator archive and, at the time of writing this article, are available directly from the primary investigator's web site (https://atmos.uw.edu/~roj/MARCUS_and_MICRE/) or by request to Roger Marchand at the University of Washington (rojmarch@u.washington.edu). Additionally, the BASTA and University of Canterbury ceilometer data are available through the Australian Antarctic Division's Data Centre (https://data.aad.gov.au/metadata/records/AAS_4292_Macquarie_Cloud_Radar and https://data.aad.gov.au/metadata/records/AAS_4292_Macquarie_Ceilometer respectively).

Acknowledgments
This work was supported by the U.S. Department of Energy Atmospheric System Research program through Grant DE-SC0016225 and NASA through Grant NNX16AM05G. The authors would like to express extra thanks to Matthew Lebsock and John Haynes from NASA Jet Propulsion Laboratory for their guidance and feedback regarding the CloudSat R05 retrievals used in the analysis. Technical and logistical support for the deployment to Macquarie Island were provided by the Australian Antarctic Division through Australian Antarctic Science Project 4292, and we thank Andrew Klekociuk, John French, Peter de Vries, Terry Egan, Nick Cartwright, and Ken Barrett for all of their assistance. We would also like to thank Adrian McDonald for providing the University of Canterbury ceilometer data used to supplement the ARM ceilometer.

References

Abel, S. J., & Boutle, I. A. (2012). An improved representation of the raindrop size distribution for single-moment microphysics schemes. *Quarterly Journal of the Royal Meteorological Society*, *138*, 2151–2162. https://doi.org/10.1002/qj.1949

Adams, N. (2009). Climate trends at Macquarie Island and expectations of future climate change in the sub-Antarctic. *Papers and Proceedings of the Royal Society of Tasmania*, *143*, 1–8. https://doi.org/10.26749/rstpp.143.1.1

Ahn, E., Huang, Y., Siems, S. T., & Manton, M. J. (2017). A comparison of cloud microphysical properties derived from MODIS and CALIPSO with in situ measurements over the wintertime Southern Ocean. *Journal of Geophysical Research: Atmospheres*, *123*, 11120–11140. https://doi.org/10.1029/2018JD028535

Battaglia, A., Rustemeier, E., Tokay, A., Blahak, U., & Simmer, C. (2010). Parsivel snow observations: A critical assessment. *The Journal of Atmospheric and Oceanic Technology*, *27*, 333–344. https://doi.org/10.1175/2009JTECHA1332.1

Bauer, M. P., Tselioudis, G., & Rossow, W. B. (2016). A new climatology for investigating storm influences in and on the extratropics. *Journal of Applied Meteorology and Climatology*, *55*(5), 1287–1303. https://doi.org/10.1175/JAMC-D-15-0245.1

Behrangi, A., Christensen, M., Richardson, M., Lebsock, M., Stephens, G., Hu man, G., et al. (2016). Status of high-latitude precipitation estimates from observations and reanalyses. *Journal of Geophysical Research: Atmospheres*, *121*, 4468–4486. https://doi.org/10.1002/2015JD024546

Behrangi, A., Lebsock, M., Wong, S., & Lambrigtsen, B. (2012). On the quantification of oceanic rainfall using spaceborne sensors. *Journal of Geophysical Research*, *117*, D20105. https://doi.org/10.1029/2012JD017979

Behrangi, A., Stephens, G., Adler, R. F., Huffman, G. J., Lambrigtsen, B., & Lebsock, M. (2014). An update on the oceanic precipitation rate and its zonal distribution in light of advanced observations from space. *Journal of Climate*, *27*, 3957–3965. https://doi.org/10.1175/JCLI-D-13-00679.1

Bodas-Salcedo, A., Hill, P. G., Furtado, K., Williams, K. D., Field, P. R., Manners, J. C., et al. (2016). Large contribution of supercooled liquid clouds to the solar radiation budget of the Southern Ocean. *Journal of Climate*, *29*, 4213–4228. https://doi.org/10.1175/JCLI-D-15-0564.1

Bodas-Salcedo, A., Mulcahy, J. P., Andrews, T., Williams, K. D., Ringer, M. A., Field, P. R., & Elsaesser, G. S. (2019). Strong dependence of atmospheric feedbacks on mixed-phase microphysics and aerosol-cloud interactions in HadGEM3. *Journal of Advances in Modeling Earth Systems*, *11*, 1735–1758. https://doi.org/10.1029/2019MS001688

Boisvert, L., Vihma, T., & Shie, C. (2020). Evaporation from the Southern Ocean estimated on the basis of AIRS satellite data. *Journal of Geophysical Research: Atmospheres*, *125*, e2019JD030845. https://doi.org/10.1029/2019JD030845

Bretherton, C., Wood, R., George, R. C., Leon, D., Allen, G., & Zheng, X. (2010). Southeast Pacific stratocumulus clouds, precipitation and boundary layer structure sampled along 20°S during VOCALS-Rex. *Atmospheric Chemistry and Physics*, *10*, 10639–10654. https://doi.org/10.5194/acp-10-10639-2010

Ceppi, P., Hwang, Y.-T., Frierson, D. M. W., & Hartmann, D. L. (2012). Southern Hemisphere jet latitude biases in CMIP5 models linked to shortwave cloud forcing. *Geophysical Research Letters*, *39*, L19708. https://doi.org/10.1029/2012GL053115

Ceppi, P., Hwang, Y.-T., Liu, X., Frierson, D. M. W., & Hartmann, D. L. (2013). The relationship between the ITCZ and the Southern Hemispheric eddy-driven jet. *Journal of Geophysical Research: Atmospheres*, *118*, 5136–5146. https://doi.org/10.1002/jgrd.50461

Chubb, T. H., Jensen, J. B., Siems, S. T., & Manton, M. J. (2013). In-situ observations of supercooled liquid clouds over the Southern Ocean during the HIAPER Pole-to-Pole Observations campaign. *Geophysical Research Letters*, *40*, 5280–5285. https://doi.org/10.1002/grl.50986

Dai, A. (2008). Temperature and pressure dependence of the rain-snow phase transition over land and ocean. *Geophysical Research Letters*, *35*, L12802. https://doi.org/10.1029/2008GL033295

Delanoë, J., Protat, A., Vinson, J.-P., Brett, W., Caudoux, C., Bertrand, F., et al. (2016). BASTA, a 95 GHz FMCW Doppler radar for cloud and fog studies. *Journal of Atmospheric and Oceanic Technology*, *33*, 1023–1038. https://doi.org/10.1029/95JD03068

Field, P. R., & Wood, R. (2007). Precipitation and cloud structure in midlatitude cyclones. *Journal of Climate*, *20*, 233–254. https://doi.org/10.1175/JCLI3998.1

Friedrich, K., Higgins, S., Masters, F. J., & Lopez, C. R. (2013). Articulating and stationary PARSIVEL disdrometer measurements in conditions with strong winds and heavy rainfall. *Journal of Atmospheric and Oceanic Technology*, *30*, 2063–2080. https://doi.org/10.1175/JTECH-D-12-00254.1

Frisch, A. S., Fairall, C. W., & Snider, J. B. (1995). Measurement of stratus cloud and drizzle parameters in ASTEX with a Ka-band radar and a microwave radiometer. *Journal of the Atmospheric Sciences*, *52*, 2788–2799. https://doi.org/10.1175/1520-0469(1995)052<2788:MOSCAD>2.0.CO;2

Gettelman, A., Hannay, C., Bacmeister, J. T., Neale, R. B., Pendergrass, A. G., Danabasoglu, G., et al. (2019). High climate sensitivity in the community Earth system model version 2 (CESM2). *Geophysical Research Letters*, *46*, 8329–8337. https://doi.org/10.1029/2019GL083978

Hande, L. B., Siems, S. T., Manton, M. J., & Belusic, D. (2012). Observations of wind shear over the Southern Ocean. *Journal of Geophysical Research: Atmospheres*, *117*, D12206. https://doi.org/10.1029/2012JD017488

Hayden, L., & Liu, C. (2018). A multiyear analysis of global precipitation combining CloudSat and GPM precipitation retrievals. *Journal of Hydrometeorology*, *19*, 1935–1952. https://doi.org/10.1175/JHM-D-18-0053.1

Haynes, J. M., L'Ecuyer, T. S., Stephens, G. L., Miller, S. D., Mitrescu, C., Wood, N. B., & Tanelli, S. (2009). Rainfall retrieval over the ocean with spaceborne W-band radar. *Journal of Geophysical Research*, *114*, D00A22. https://doi.org/10.1029/2008JD009973

Huang, Y., Siems, S. T., Manton, M. J., Rosenfeld, D., Marchand, R., McFarquhar, G. M., & Protat, A. (2016). What is the role of sea surface temperature in modulating cloud and precipitation properties over the Southern Ocean? *Journal of Climate*, *29*, 7453–7476. https://doi.org/10.1175/JCLI-D-15-0768.1

Huffman, G. J., & Bolvin, D. T. (2013). Version 1.2 GPCP one-degree daily precipitation data set documentation. Retrieved from ftp://precip.gsfc.nasa.gov/pub/1dd-v1.2/1DD_v1.2_doc.pdf

Hwang, Y., & Frierson, D. (2013). Link between the double-Intertropical convergence Zone problem and cloud bias over Southern Ocean. *Proceedings of the National Academy of Sciences of the United States of America*, *110*, 4935–4940. https://doi.org/10.1073/pnas.1213302110

Kay, J. E., Wall, C., Yettella, V., Medeiros, B., Hannay, C., Caldwell, P., & Bitz, C. (2016). Global climate impacts of fixing the Southern Ocean shortwave radiation bias in the community Earth system model (CESM). *Journal of Climate*, *29*, 4617–4636. https://doi.org/10.1175/JCLI-D-15-0358.1

Klepp, C., Michel, S., Protat, A., Burdanowitz, J., Albern, N., Kähnert, M., et al. (2018). OceanRAIN, a new in-situ shipboard global ocean surface-reference dataset of all water cycle components. *Scientific Data*, *5*, 180122. https://doi.org/10.1038/sdata.2018.122

Lang, F., Huang, Y., Protat, A., Truong, S. C. H., Siems, S. T., & Manton, M. J. (2021). Shallow convection and precipitation over the Southern Ocean: A case study during the CAPRICORN 2016 field campaign. *Journal of Geophysical Research: Atmospheres*, *126*, e2020JD034088. https://doi.org/10.1029/2020JD034088

Lang, F., Huang, Y., Siems, S. T., & Manton, M. J. (2018). Characteristics of the marine atmospheric boundary layer over the Southern Ocean in response to the synoptic forcing. *Journal of Geophysical Research: Atmospheres*, *123*, 7799–7820. https://doi.org/10.1029/2018JD028700

Lang, F., Huang, Y., Siems, S. T., & Manton, M. J. (2020). Evidence of a diurnal cycle in precipitation over the Southern Ocean as observed at Macquarie island. *Atmosphere*, *11*(2), 181. https://doi.org/10.3390/atmos11020181

Lebsock, M. D., & L'Ecuyer, T. S. (2011). The retrieval of warm rain from CloudSat. *Journal of Geophysical Research*, *116*, D20209. https://doi.org/10.1029/2011JD016076

Löffler-Mang, M., & Joss, J. (2000). An optical disdrometer for measuring size and velocity of hydrometeors. *Journal of Atmospheric and Oceanic Technology*, *17*(2), 130–139. https://doi.org/10.1175/1520-0426(2000)017<0130:AODFMS>2.0.CO

Mace, G. G., & Protat, A. (2018a). Clouds over the Southern Ocean as observed from the R/V investigator during CAPRICORN. Part I: Cloud occurrence and phase partitioning. *Journal of Applied Meteorology and Climatology*, *57*, 1783–1804. https://doi.org/10.1175/JAMC-D-17-0194.1

Mace, G. G., & Protat, A. (2018b). Clouds over the Southern Ocean as observed from the R/V investigator during CAPRICORN. Part II: The properties of nonprecipitating stratocumulus. *Journal of Applied Meteorology and Climatology*, *57*(8), 1805–1823. https://doi.org/10.1175/JAMC-D-17-0195.1

Mace, G. G., Protat, A., Humphries, R. S., Alexander, S. P., McRobert, I. M., Ward, J., et al. (2021). Southern Ocean cloud properties derived from CAPRICORN and MARCUS data. *Journal of Geophysical Research: Atmospheres*, *126*, e2020JD033368. https://doi.org/10.1029/2020JD033368

Manton, M. J., Huang, Y., & Siems, S. T. (2020). Variations in precipitation across the Southern Ocean. *Journal of Climate*, *33*(24), 10653–10670. https://doi.org/10.1175/JCLI-D-20-0120.1

Marchand, R., Mace, G. G., Ackerman, T., & Stephens, G. (2008). Hydrometeor detection using Cloudsat—An Earth-Orbiting 94-GHz cloud radar. *Journal of Atmospheric and Oceanic Technology*, *25*(4), 519–533. https://doi.org/10.1175/2007JTECHA1006.1

Marshall, J. S., & Palmer, W. M. (1948). The distribution of raindrops with size. *Journal of Meteorology*, *5*, 165–166. https://doi.org/10.1175/1520-0469(1948)005<0165:TDORWS>2.0.CO;2

McFarquhar, G. M., Bretherton, C. S., Marchand, R., Protat, A., DeMott, P. J., Alexander, S. P., et al. (2021). Observations of clouds, aerosols, precipitation, and surface radiation over the Southern Ocean: An overview of CAPRICORN, MARCUS, MICRE, and SOCRATES. *Bulletin of the American Meteorological Society*, *102*(4), E894–E928. https://doi.org/10.1175/BAMS-D-20-0132.1

Naud, C. M., Posselt, D. J., & van den Heever, S. C. (2014). A CloudSat-CALIPSO view of cloud and precipitation properties across cold fronts over the global oceans. *Journal of Climate*, *28*(17), 6743–6762. https://doi.org/10.1175/JCLI-D-15-0052.1

Nešpor, V., & Sevruk, B. (1999). Estimation of wind-induced error of rainfall gauge measurements using a numerical simulation. *Journal of Atmospheric and Oceanic Technology*, *16*(4), 450–464. https://doi.org/10.1175/1520-0426(1999)016<0450:EOWIEO>2.0.CO;2

Orr, B. W., Kropfli, R. A. (1999). A method for estimating particle fall velocities from vertically pointing Doppler radar. *Journal of Atmospheric and Oceanic Technology*, *16*, 29–37. https://doi.org/10.1175/1520-0426(1999)016<0029:AMFEPF>2.0.CO;2

Pauling, A. G., Bitz, C. M., Smith, I. J., & Langhorne, P. J. (2016). The response of the Southern Ocean and Antarctic sea ice to freshwater from ice Shelves in an Earth system model. *Journal of Climate*, *29*(5), 1655–1672. https://doi.org/10.1175/jcli-d-15-0501.1

Protat, A., Bouniol, D., O'Connor, E. J., Klein Baltink, H., Verlinde, J., & Widener, K. (2011). CloudSat as a global radar calibrator. *Journal of Atmospheric and Oceanic Technology*, *28*(3), 445–452. https://doi.org/10.1175/2010JTECHA1443.1

Raupach, T. H., & Berne, A. (2015). Correction of raindrop size distributions measured by Parsivel disdrometers, using a two-dimensional video disdrometer as a reference. *Atmospheric Measurement Techniques*, *8*, 343–365. https://doi.org/10.5194/amt-8-343-2015

Sallée, J.-B., Shuckburgh, E., Bruneau, N., Meijers, A. J. S., Bracegirdle, T. J., Wang, Z., & Roy, T. (2013). Assessment of Southern Ocean water mass circulation and characteristics in CMIP5 models: Historical bias and forcing response. *Journal of Geophysical Research: Oceans*, *118*, 1830–1844. https://doi.org/10.1002/jgrc.20135

Savic-Jovcic, V., & Stevens, B. (2008). The structure and mesoscale organization of precipitating stratocumulus. *Journal of the Atmospheric Sciences*, *65*(5), 1587–1605. https://doi.org/10.1175/2007JAS2456.1

Savina, M., Schäppi, B., Molnar, P., Burlando, P., & Sevruk, B. (2012). Comparison of a tipping-bucket and electronic weighing precipitation gage for snowfall. *Atmospheric Research*, *103*, 45–51. https://doi.org/10.1016/j.atmosres.2011.06.010

Schneider, D., & Reusch, D. B. (2016). Antarctic and Southern Ocean surface temperatures in CMIP5 models in the context of the surface energy budget. *Journal of Climate*, *29*, 1689–1716. https://doi.org/10.1175/JCLI-D-15-0429.1

Sevruk, B.(1996). Adjustment of tipping-bucket precipitation gauge measurements. *Atmospheric Research*, *42*, 1–4. https://doi.org/10.1016/0169-8095(95)00066-6

Silber, I., Fridlind, A. M., Verlinde, J., Ackerman, A. S., Cesana, G. V., & Knopf, D. A. (2021). *Atmospheric Chemistry and Physics*, *21*, 3949–3971. https://doi.org/10.5194/acp-21-3949-2021

Sims, E. M., & Liu, G. (2015). A parameterization of the probability of snow-rain transition. *Journal of Hydrometeorology*, *16*, 1466–1477. https://doi.org/10.1175/JHM-D-14-0211.1

Skofronick-Jackson, G., Petersen, W. A., Berg, W., Kidd, C., Stocker, E. F., Kirschbaum, D. B., et al. (2017). The global precipitation measurement (GPM) mission for Science and Society. *Bulletin of the American Meteorological Society*, *98*(8), 1679–1695. https://doi.org/10.1175/BAMS-D-15-00306.1

Stephens, G. L. J., LiWild, M. C. A., Clayson, N., Loeb, S., Kato, T. L., Ecuyer, P. W., et al. (2012). An update on Earth's energy balance in light of the latest global observations. *Nature Geoscience*, *5*, 691–696. https://doi.org/10.1038/ngeo1580

Sui, C.-H., Lau, K.-M., Takayabu, Y. N., & Short, D. A. (1997). Diurnal variations in tropical oceanic cumulus convection during TOGA COARE. *Journal of the Atmospheric Sciences*, *54*(5), 639–655. https://doi.org/10.1175/1520-0469(1997)054<0639:DVITOC>2.0.CO;2

Tan, J., Huffman, G. J., Bolvin, D. T., & Nelkin, E. J. (2019). Diurnal cycle of IMERG V06 precipitation. *Geophysical Research Letters*, *46*, 584–592. https://doi.org/10.1029/2019GL085395

Tanelli, S., Durden, S. L., Im, E., Pak, E., Reinke, D. G., Partain, P., et al. (2008). CloudSat's cloud profiling radar after two years in orbit: Performance, calibration, and processing. *IEEE Transactions on Geoscience and Remote Sensing*, *46*(11), 3560–3573. https://doi.org/10.1109/tgrs.2008.2002030

Tao, W., Simpson, J., Sui, C. H., Ferrier, B., Lang, S., Scala, J., et al. (1993). Heating, Moisture, and Water Budgets of Tropical and Midlatitude Squall Lines: Comparisons and Sensitivity to Longwave Radiation, *Journal of Atmospheric Sciences*, *50*(5), 673-690. https://doi.org/10.1175/1520-0469(1993)050%3C0673:HMAWBO%3E2.0

Tokay, A., Petersen, W. A., Gatlin, P., & Wingo, M. (2013). Comparison of raindrop size distribution measurements by collocated disdrometers. *Journal of Atmospheric and Oceanic Technology*, *30*(8), 1672–1690. https://doi.org/10.1175/JTECH-D-12-00163.1

Trenberth, K., & Fasullo, J. (2010). Simulation of present-day and twenty-first century energy budgets over the Southern Ocean. *Journal of Climate*, *23*, 440–454. https://doi.org/10.1175/2009jcli3152.1

Tridon, F., & Battaglia, A. (2015). Dual-frequency radar Doppler spectral retrieval of rain drop size distributions and entangled dynamics variables. *Journal of Geophysical Research: Atmospheres*, *120*, 5585–5601. https://doi.org/10.1002/2014JD023023

Von Storch, H., & Zwiers, F. W. (2002). *Statistical analysis in climate research*. Cambridge University Press.

Wang, Z., Belusic, D., Huang, Y., Siems, S., & Manton, M. (2016). Understanding orographic effects on surface observations at Macquarie island. *Journal of Applied Meteorology and Climatology*, *55*, 2377–2395. https://doi.org/10.1175/JAMC-D-15-0305.1

Wang, Z., Siems, S., Belusic, D., Manton, M., & Huang, Y. (2015). A climatology of the precipitation over the Southern Ocean as observed at Macquarie island. *Journal of Applied Meteorology and Climatology*, *54*, 2321–2337. https://doi.org/10.1175/jamc-d-14-0211.1

Watters, D., & Battaglia, A. (2019). The summertime diurnal cycle of precipitation derived from IMERG. *Remote Sensing*, *11*(15), 1781. https://doi.org/10.3390/rs11151781

Wood, N. B., L'Ecuyer, T. S., Heymsfield, A. J., Stephens, G. L., Hudak, D. R., & Rodriguez, P. (2014). Estimating snow microphysical properties using collocated multisensor observations. *Journal of Geophysical Research: Atmospheres*, *119*, 8941–8961. https://doi.org/10.1002/2013JD021303

Wood, R. (2006). Rate of loss of cloud droplets by coalescence in warm clouds. *Journal of Geophysical Research*, *111*, D21205. https://doi.org/10.1029/2006JD007553

Wood, R. (2012). Stratocumulus clouds. *Monthly Weather Review*, *140*(8), 2373–2423. https://doi.org/10.1175/MWR-D-11-00121.1

Xie, P., & Arkin, P. A. (1997). Global precipitation: A 17-year monthly analysis based on gauge observations, satellite estimates, and numerical model outputs. *Bulletin of the American Meteorological Society*, *78*, 2539–2558. https://doi.org/10.1175/1520-0477(1997)078<2539:GPAYMA>2.0.CO;2

Yang, S., & Smith, E. A. (2006). Mechanisms for diurnal variability of global tropical rainfall observed from TRMM. *Journal of Climate*, *19*(20), 5190–5226. https://doi.org/10.1175/JCLI3883.1

Zelinka, M. D., Myers, T. A., McCoy, D. T., Po-Chedley, S., Caldwell, P. M., Ceppi, P., et al. (2020). Causes of higher climate sensitivity inCMIP6 models. *Geophysical Research Letters*, *47*, e2019GL085782. https://doi.org/10.1029/2019GL085782

Zweifel, A., Sevruk, B., (2002). Comparative accuracy of solid precipitation measurement using heated recording gauges in the Alps. In *WCRP Workshop on determination of solid precipitation in cold climate regions*. Fairbanks.

References From the Supporting Information

Gunn, R., & Kinzer, G. D. (1949). The terminal velocity of fall for water droplets in stagnant air, *Journal of Atmospheric Sciences*, *6*(4), 243-248. https://doi.org/10.1175/1520-0469(1949)006%3C0243:TTVOFF%3E2.0

Jaffrain, J., & Berne, A. (2011). Experimental Quantification of the Sampling Uncertainty Associated with Measurements from PARSIVEL Disdrometers, *Journal of Hydrometeorology*, *12*(3), 352-370. https://doi.org/10.1175/2010JHM1244.1

Locatelli, J. D., & Hobbs, P. V. (1974). Fall speeds and masses of solid precipitation particles, *J. Geophys. Res.*, *79*(15), 2185– 2197, https://doi.org/10.1029/JC079i015p02185

Magono, C. & Nakamura, T. (1964). Aerodynamic Studies of Falling Snowflakes, *Journal of the Meteorological Society of Japan*, *43*(3), 139-148.